Broadband Nanosensing using Heterodyne Interferometry

by

Bennett Landman

Submitted to the Department of Electrical Engineering and Computer Science
in partial fulfillment of the requirements for the degree of

Master of Engineering in Electrical Engineering and Computer Science

at the

MASSACHUSETTS INSTITUTE OF TECHNOLOGY

February 2002

Author .....
Department of Electrical Engineering and Computer Science
January 9, 2002

Certified by..
.....
Dennis Freeman
Associate Professor
Thesis Supervisor

Accepted by ....
.....
Arthur C. Smith
Chairman, Department Committee on Graduate Theses

Broadband Nanosensing using Heterodyne Interferometry

by

Bennett Landman

Submitted to the Department of Electrical Engineering and
Computer Science
on January 9, 2002, in partial fulfillment of the
requirements for the degree of
Master of Engineering in Electrical Engineering and Computer Science

Abstract

Interferometric and bright field microscopy methods for measuring vibrational, periodic motions have been well established. We extend existing measurement techniques to encompass detection of broadband, aperiodic motions of microscopic beads along one dimension. In the device, a coherent 488 nm laser beam is split into two beams with a relative frequency shift of 3.4 MHz. The beams are overlapped on a target slide to form a rolling interference pattern. A latex bead is placed in the pattern, and a photomultiplier incoherently collects the scattered light. The amount of light scattered by the bead varies sinusoidally due to the rolling interference pattern. Motions of the bead modulate the phase of the sinusoid. The detected signal is sampled at 10 megasamples/second and digitally phase demodulated. Over a frequency bandwidth of 10 kHz to 1 MHz, a broadband rms noise density of 19 pm/$\sqrt{\text{Hz}}$ was observed for a 1.5 μm diameter bead. Due to sub-500 Hz equipment vibration, the mean rms noise level was 101 pm/$\sqrt{\text{Hz}}$ over DC to 100 kHz. The system would allow measurements as small as 30 nm for an observation bandwidth of 2.5 MHz. Further enhancements to increase the power of collected light could extended the resolution to characterize the Brownian motion of beads in the tectorial membrane.

Thesis Supervisor: Dennis Freeman
Title: Associate Professor

Acknowledgments

First, I would like to thank my advisor, Dennis Freeman, for his inspiration, confidence and persistent support. He has helped solve the most perplexing problems. His enthusiasm permeates the eighth floor and has helped make this a wonderful (yet sleepless) experience. I greatly appreciate the advice of Charles Sodini and Howard Schrobe, who guided my thesis aspirations and introduced me to Professor Freeman.

My fellow eighth floor students have provided invaluable assistance over the past year. With extreme patience, Stan Hong has taken countless hours away from his research to explain a myriad of ideas and has proofread this work with insightful comments. A.J. Aranyosi has been the utmost authority on how to get things done in lab. Thank you for putting up with nearly continuous questions. Andy Copeland and Salil Desai loaned me key components from their work at the last minute (sometimes before they knew that they had). Janice Balzar, the lab secretary, always came through despite my unconscious attempts to thwart her. Thanks to Amy Englehart for being here during those lonely morning hours. From U.C. Berkeley, Jen Nickel and Temina Madon have been extremely helpful editing this document.

MIT would not have been what it was without friends whose support has preserved most of the sanity in this crazy life we have lived. I thank all of those people who I have been fortunate enough to call my friends.

Thanks to Mom and Dad (Petra and Gary Landman) for always supporting me in everything that I do. Mom, the care packages and phone calls have meant more to me than I could ever tell you. Dad, I keep your writing advice close at hand — see you can teach a computer nerd something. Rebeccah, you are the world's best sister. Zach, thanks for making me the most popular big brother in high school.

To close, I would like to thank my wife, Melissa Ohsfeldt Landman. She has put up with more than I can imagine during this extended crunch period and has encouraged me to focus my thoughts so I could rejoin her as quickly as possible.

Contents

List of Figures

Chapter 1

Introduction

1.1 Motivation

Engineering systems are getting smaller and harder to see. New microfabrication techniques are narrowing the boundaries between molecules and machines. Accelerometers that are smaller than the diameter of a human hair are now commonplace.

To understand the mechanics of these new machines, we require technologies that can measure minute motions without interfering with operation. Light microscopy is a powerful, minimally invasive tool, but diffraction effects limit the achievable resolution to half the wavelength of the light[1].[1] A method of using light microscopy to achieve nanometer resolution with image processing techniques has been demonstrated[2]. This method requires that motion be periodic and that stroboscopic illumination be used to freeze motion. This method cannot be used to detect nanometer motions over a broad frequency range.

An alternative approach to achieving high resolution motion measurements has been to use optical interference to generate fringes that facilitate higher contrast detection[3]. Laser interferometry encompasses a class of methods that have proven extremely effective for determining displacement, flow velocity, and vibrational motion. Within the general class of methods, there are two distinct signal detection mod-

[1]The average wavelength of visible light is approximately 500 nm.

els: heterodyne and direct detection. Heterodyne detection interferometric methods interfere a probing beam with a reference beam[4]. The probing beam and reference beams are at slightly different frequencies, so their interference pattern "optically beats." The motion of the bead introduces a phase shift into the beating signal. In direct detection interferometry, beams are overlapped to form fringe patterns on a target[4]. The position of the target within the fringe pattern determines the intensity of light scattered. The light is incoherently collected by a detector.

This research develops an interferometric system that expands on existing vibration measurement technologies to encompass broadband nanosensing. Previous systems were developed to measure periodic ranges of movement at a specific frequency[5, 6]. As such, they may be categorized as narrow-band methods. This research focuses on the ability to detect aperiodic motions over a broad range of frequencies. Interferometric illumination is used to create an "optical radio" that can detect aperiodic, broadband motions as shown in Figure 1-1.

1.2 Narrow-Band Interferometric Techniques

In 1964, Yeh and Cummins observed that the frequency of light changed as it passed though a stream of moving particles[7]. The interaction of the moving particles with the light introduced a Doppler shift in the scattered light. By carefully measuring the amount of frequency shift, they were able to determine stream velocity. Steady advances and refinements of their technique have lead to a variety of direct and heterodyne methods that are collectively known as laser Doppler methods[3]. These methods routinely achieve 20 μm spatial accuracy with microsecond temporal resolution. A key advantage of using interferometric methods over physical contact methods is that the particle flow is not disturbed during observation. However, the methods are not without drawbacks; the particle stream must be optically transparent and additional doping may be necessary to increase the density of scattering particles.

In 1980, Buunen demonstrated a heterodyne laser Doppler velocity meter to measure vibrational motions of a cat tympanic membrane[5]. One beam was used to

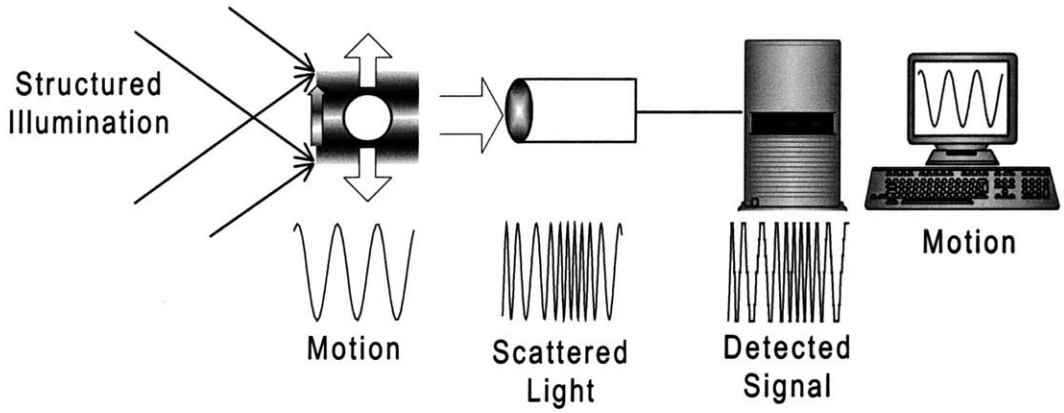

Figure 1-1: Conceptual schematic. The device is essentially an "optical radio." Structured illumination, lasers, overlap to form a rolling interference pattern. In the region of overlap, indicated by the gradient, the brightness varies sinusoidally with time and position. A target, represented by the white dot, is placed in the rolling fringe pattern. If the target is stationary, the scattered light intensity oscillates sinusoidally. Target movement along the axis of fringe variation introduces a phase shift in the oscillations of the scattered light. The light is collected by a photomultiplier, represented by a rectangle with an oval aperture. The photomultiplier current is band-limited and digitized. A computer utilizes phase demodulation algorithms to determine the motion of the target in the fringe pattern.

illuminate a 100 μm spot on the membrane while researchers stimulated the membrane with acoustic waves. Membrane motion generated a Doppler shift in the light scattered from its surface. Scattered light was interfered with a reference beam on a detector. The reference beam was frequency shifted by 400 kHz, so the Doppler shifted signal was modulated at 400 kHz. The detected signal was electronically enhanced by filtering, averaging, and time sensitive detection. The Buunen detection method was able to measure vibrations on the order of 0.1 nm.[2] Their maximum observable frequency was 2.24 kHz.

In 1987, van Netten presented a direct detection laser interferometry microscope for use on fish lateral line organs[6]. He illuminated a 1.15 μm diameter polymer bead with a fringe pattern. The heterodyne frequency of the fringe pattern was 400 kHz and the fringe spacing was approximately 0.7 μm. This device detected vibrational displacements from 0.3 nm to 300 nm with observable motion frequencies of 10 to 500 Hz. A glass sphere mounted on a piezoelectric device was used to stimulate vibrations.

1.3 Broadband Laser Interferometry

When particle motion cannot be assumed to be periodic, the methods developed by Buunen and van Netten to generate interference patterns and detect scattered light can still be used[5, 6]. However, different signal processing methods are required. Furthermore, temporal correlation cannot always be exploited to reduce noise. This research develops a technique for measuring motion that can be tuned to exchange observation bandwidth for spatial resolution. The fundamental benefit from this method is that the interferometer can be adjusted to suit a range of applications.

One such application of the broadband laser interferometer is in the study of hearing. Research has shown that humans can detect sound vibrations with amplitudes as small as 1 pm[5]. The tectorial membrane, a thin gelatinous structure in the ear, has been shown to play a key role in producing the vibrations that are detected by

[2]As a matter of perspective, the Bohr model of a hydrogen atom has a diameter of 0.1 nm.

the sensory hair cells. Vibration sensing interferometers have been used to determine the frequency responses of the structure, but some material properties, such as the stiffness of the gel, remain elusive.

One method of measuring stiffness is to apply a force and measure displacement. If the material behaves as an elastic spring, then displacement will be linear with force. If the material behaves as a viscous fluid, then force will be proportional to velocity. A gel, such as the tectorial membrane, has both viscous and elastic properties. Mechanical properties of gels which are determined by the gel's cross-linked network of polymeric macromolecules, are nonlinear. We therefore seek methods to measure mechanical properties of the tectorial membrane for small forces and small displacement. The ultimate limiting range of detectable movement would be determined by the Brownian of the system. Using the force-displacement method, displacements of the tectorial membrane as small as hundreds of nm have been measured in response to forces as small as tens of nN[8]. However these forces and displacements are orders of magnitude greater than those that occur in hearing.

An alternative approach for measuring the visco-elastic behavior in a gel is to let thermal energy drive Brownian motion. The material properties may be calculated from the statistics of gel motion given the random thermal energy. Narrow-band measuring systems could not be used in this experiment because the motion is not driven at a particular frequency. Furthermore, the range of Brownian motion drastically decreases with increasing target size, so localized measurements of motion are necessary. A broadband laser interferometer similar to this research design would enable the measurement of visco-elastic properties through statistical analysis of Brownian motion.

Chapter 2

Survey of Technology

The primary components of the interferometer design are a fringe projector, a scattering target, and a detection system. The fringe projector overlaps two coherent beams of similar wavelengths in a volume of space. The beams constructively and destructively interfere to form a three dimensional volume of bright and dark fringes. A target, such as a small bead, is placed in the illuminated area and interacts with and scatters light. The measured scattering intensity depends on the bead position and angle of observation. A detection system collects the scattered light and infers the target position.

As Figure 2-1 illustrates, bead and fringe movements in the out-of-plane directions will not change the illumination of the bead since the fringe pattern varies along only one axis. Changes in the intensity of the scattered light are caused by movements of the particle or the fringe pattern. Therefore, a two beam fringe projection system is limited to measuring motions in one dimension.[1]

The intensity of scattered light is proportional to the incident light on the sphere during the measurement interval. For example, the light is at a minimum when the bead is mostly covered by dark fringe bands and at a maximum when it is covered by light fringe bands. If the fringe pattern and sphere are assumed to be stationary

[1]Multidimensional measurement systems are possible with systems of more than two beams. This research focuses solely on the case of two stationary beams. A discussion of multi-beam possibilities is presented in the closing remarks.

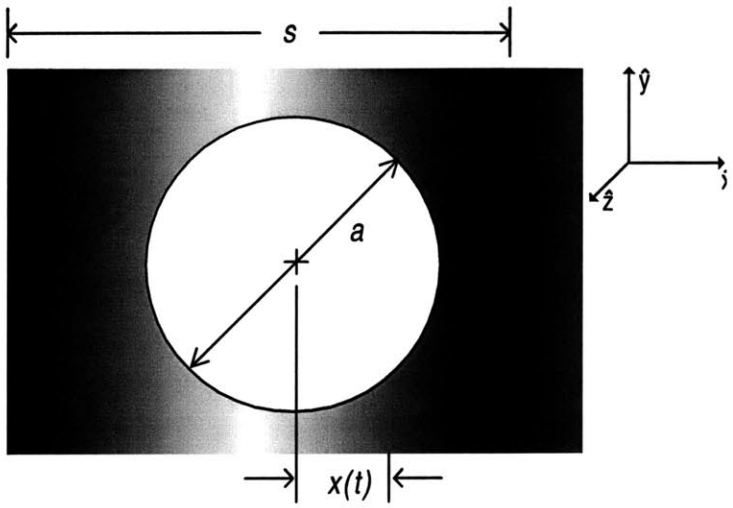

Figure 2-1: Two-dimensional model of a sphere in a fringe pattern. A sphere is represented by a disc of a diameter, a. The axis of fringe variation is represented by $\hat{x}$. The distance between consecutive fringe minima is the fringe period, s. Sphere position is distance from the center of the sphere to a fixed point in space that is arbitrarily set to the initial location of the nearest band of median fringe intensity. Each $\hat{y}$-$\hat{z}$ plane represents a plane of constant fringe intensity. Each point on the surface of the sphere is illuminated by the intensity of the fringe pattern at that point. The range in intensity of scattered light was estimated using the two-dimensional model (the disc model), but a three-dimensional model was used to calculate the actual scattering functions.

over the measurement period, then the scattered light will vary with the position of the sphere relative to the fringes. Thus, the motion of the sphere may be determined from the scattered light[3].

2.1 Fringe Projection

2.1.1 Interference

Techniques for generating well-defined fringes have been commonly used in laser interferometry[3]. Fringe patterns are generated by interfering coherent light beams of similar frequencies. Bright areas are formed in the region where the electric fields constructively interfere and dark areas are formed where they destructively interfere. If the beam wave fronts are sufficiently planar and the optical frequencies well-defined, lines of alternating brightness will form at an angle bisecting the angle of intersection (Figure 2-2). The fringe spacing depends on the plane of observation and is given by

$$s = \frac{\lambda}{2n \sin \alpha \cos \phi} \tag{2.1}$$

where λ is the optical wavelength, n is the index of refraction of the medium, α is the half angle of beam separation, and ϕ is the angle of rotation between the plane containing the beams and the plane containing the bisector of the beams and the axis of fringe variation. This relation is plotted in Figure 2-3. When the beams are of exactly the same frequency, the pattern is a standing wave and the envelope is stationary in time. If the beams are of different frequencies, then the bright and dark bands roll at the rate of frequency separation.

Figure 2-4 illustrates effects of non-planar wave fronts on fringe formation. In order to achieve planar wave fronts, beams are typically overlapped at their waists. The fringes will be significantly distorted if misalignment in optics causes the beams to overlap where the wave fronts differ from planar. Spherical aberration in the optics causes divergence in the beams that leads to non-uniform fringes. Furthermore, if the path lengths of the beams differ by more than the light source coherence length, the

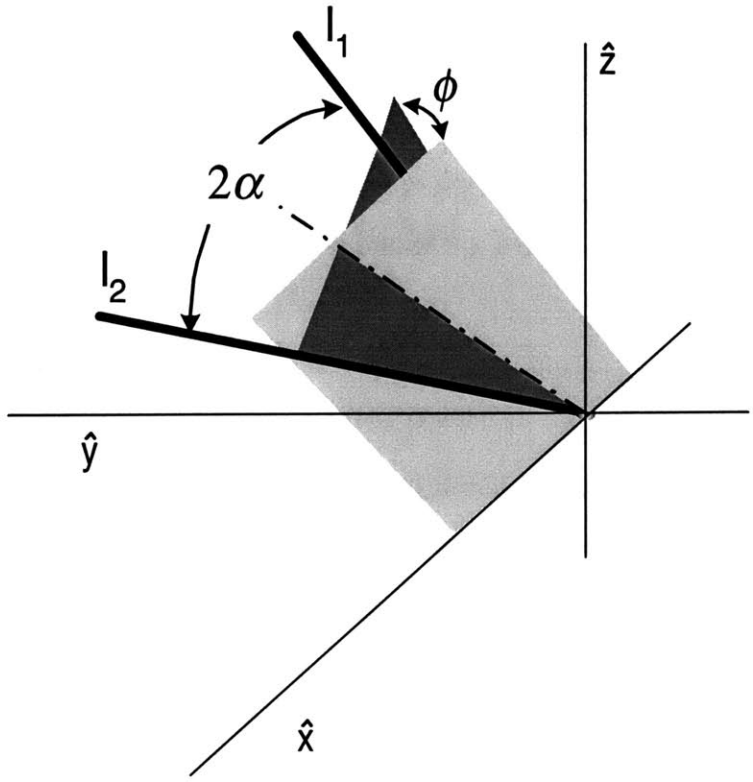

Figure 2-2: Fringe formation. When two coherent beams of sufficiently similar frequencies (l_1 and l_2) overlap, they form fringes. The figure shows a reference frame relative to the fringes with the $\hat{x} - \hat{y}$ plane as the plane of observation and fringe intensity varying only along $\hat{x}$. The half beam separation angle, α, is half of the angle between the beams in the plane containing the two beams (dark gray shading). The rotation angle, ϕ, is the angle of rotation between the plane containing the beams (dark gray shading) and the plane that contains the bisector of the beams (dotted centerline) and the x-axis ($\hat{x}$) (plane indicated by light gray shading).

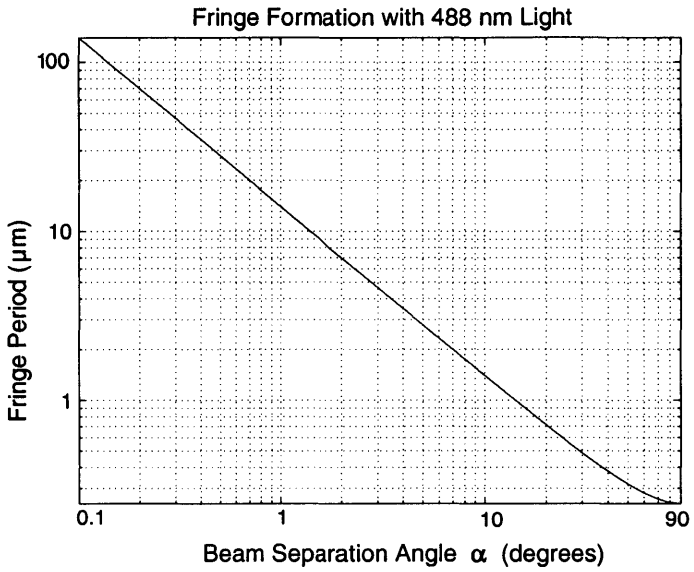

Figure 2-3: Fringe period with beam separation. The relation between fringe period and beam separation is shown for an index of refraction of 1 and rotation angle of 0 degrees.

beams will not fully interfere and the contrast between the light and dark fringes will decrease[3].

2.1.2 Beam Waist Formation

The waist of a beam occurs very close to the location where the beam is in focus. The diffraction limited diameter at the waist is approximately

$$d \approx \frac{4\lambda f}{\pi D} \tag{2.2}$$

where λ is the wavelength of light, f is the focal length used to focus the beam, and D is the diameter of the collimated beam before it was focused[6].

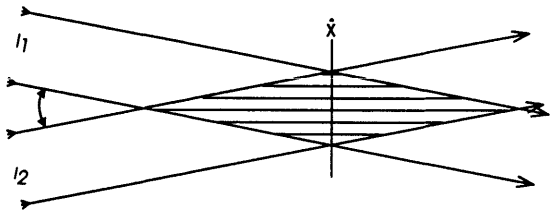

(a) Ideal fringes.

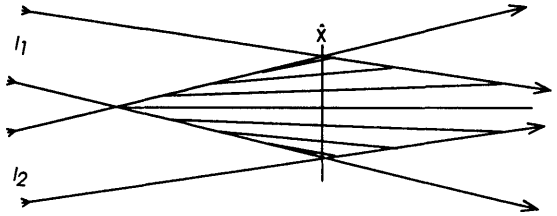

(b) Fringes from divergent beams.

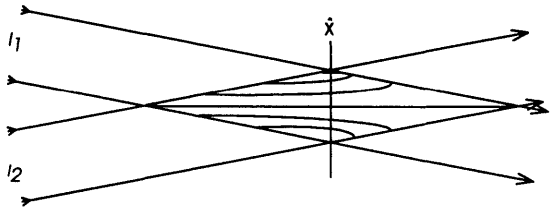

(c) Fringes from non-planar beams.

Figure 2-4: Illustration of fringe distortion. When two planar beams of the same frequency overlap, the wave fronts interfere to form straight fringes (a). Straight, non-parallel fringes are formed if the overlapping beams are divergent as in (b). If the beam wave fronts are not planar, then fringe patterns may be curved as well as skew (c).

2.2 Optical Scattering

2.2.1 Mie Scattering

Determining the optical scattering properties of a particle involves calculating the potential function at all points in space due to interaction of the particle with an incident wave. The use of a spherical target greatly simplifies the problem since Mie developed an exact analytical solution for a single beam scattering off of a sphere[9]. The amount of scattered light has been found to depend on the ratio of the index of refraction of the sphere to that of the medium and a sizing parameter given by

$$x = \frac{2\pi a}{\lambda} \tag{2.3}$$

where a is the diameter of the target sphere. In general, scattering intensity is a function of scattering angle, orientation angle, and polarization of incident radiation (Figure 2-5). Symmetry constraints for scattering off a sphere dictate that the absolute polarization and orientation angles are not relevant. Rather, the polarization as observed in a scattering plane and the scattering angle are sufficient.

The scattering of more complicated waves may be treated as a superposition of component waves. The scattering function of unpolarized light may be found by averaging the scattering functions for both parallel and perpendicular polarized light. Figure 2-6 illustrates two different scattering functions that were computed with code adapted from Barnett's "Mie Scattering Toolbox"[10].

For small spheres, the greatest scattering intensity is generally in the same direction as the incident light which is represented as higher intensity at the low angles in Figure 2-6. Unfortunately, there is also a large amount of unscattered light at low angles that makes separating the scattering signal from the illumination difficult. Scattering intensities typically decrease with increasing angle in a ripple-like manner, yet increase to local maximum near back scattering angles (180 degrees). The range of scattering intensity increases with the particle sizing parameter (Equation 2.3). Large particle scattering functions tend to vary more with angle than those of smaller ones.

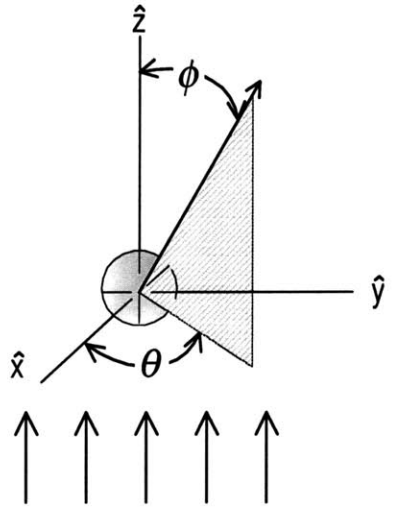

Figure 2-5: Model of scattering off a sphere. Radiation is incident perpendicular to the $\hat{x} - \hat{y}$ plane in the positive $\hat{z}$ direction as indicated by the series of arrows at the base of the figure. Light is scattered in all directions. One particular ray is indicated by the dark arrow. The scattering angle, ϕ, is the angle between $\hat{z}$ and the ray. The orientation angle, θ, is relative to the coordinate system. The scattering plane (indicated with shading) is the plane defined by the ray and $\hat{z}$ axis.

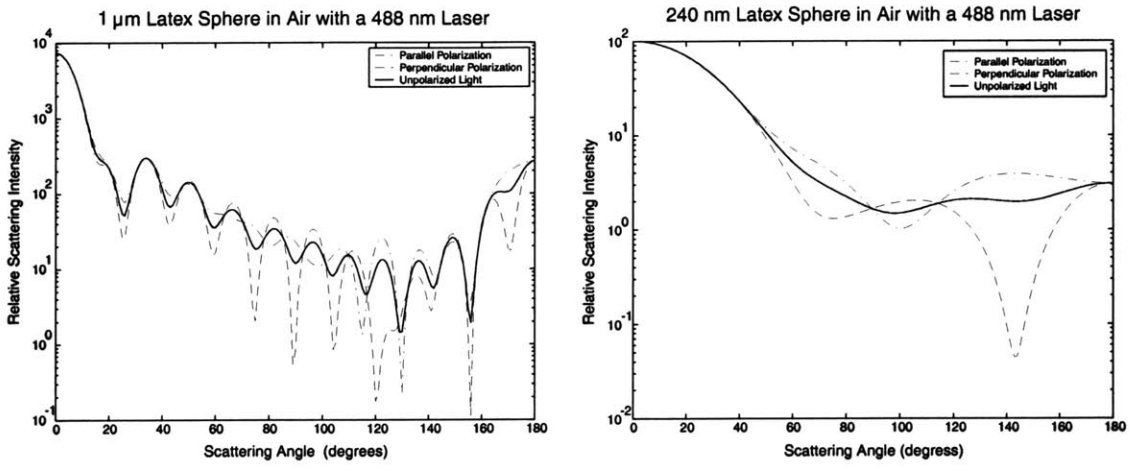

Figure 2-6: Examples of scattering profiles. The left figure shows the scattering intensity of a 1 μm diameter latex particle in air when illuminated with 488 nm light. The size parameter is approximately 12.9 and the index of refraction is 1.59. The right figure shows the scattering intensity of a 240 nm latex sphere in water when illuminated with 488 nm light. The size parameter is approximately 3. The values of the scattering functions represent the relative amount of power scattered per angle when compared the angles from the same target.

The absolute magnitudes of the angular scattering calculations are only meaningful when compared to other angles for the same target. To find the absolute amount of power scattered, the scattering cross-section must be computed. The scattering cross-section is the area of the incident beam that contains an amount of light equal to that which is scattered by the sphere. With the relative proportion of scattering per angle and the total amount of energy scattered, the amount of energy scattered per angle can be computed. When using a lens to observe scattering, only a conical section of light may collected. The scattering function may be integrated to compute the total amount of light that can be collected with a lens.

2.2.2 Modulation Effects

In general, scattered light from a bead in a rolling fringe pattern is a combination of fixed intensity signal (the DC component) and an oscillatory signal (the AC component). As a bead moves in a fringe pattern, the intensity of scattered light changes

with position. Since light intensity is never negative and a target will never be completely covered in an absolutely dark or bright band, the scattered light will have a DC offset. The ratio of the peak-to-peak values of the AC signal to twice the DC offset is defined as the modulation visibility.[3] It is a measure of the amount of signal power that the scattering signal carries. The modulation visibility is estimated from the disc model (Figure 2-1) by averaging the integral of a fringe pattern over a the cross-sectional area of a target. It is found to be

$$V = |\frac{2J_1(\pi a/s)}{\pi a/s}| \tag{2.4}$$

where J_1 is a first order Bessel function of the first kind.

While the intensity of the reflected light is determined by the illumination and the properties of the sphere, the motion signal strength in the light signal depends also on the size of the sphere and spacing of the fringe pattern. If the fringe period is very small compared to the sphere diameter, then many fringes will overlap the sphere and the scattering intensity will only vary slightly with sphere movement because only a small fraction of the illumination will change. If the fringe period is large compared to the sphere, then larger sphere movements are required to generate detectable changes in the scattering intensity[3] (Figure 2-7).

For a given sphere and cone of observation, the measured intensity of scattered light will be proportional to the total incident light on the sphere. The scattering signal may be characterized by the relationship between the sphere cross-section and illumination pattern. Without loss of generality, the position of the sphere in a stationary fringe pattern is measured from a reference position that is half way between the initially nearest light and dark fringes. The sin function is periodic with 2π, so any offset in $x(t)$ of a integer multiple of s will not change the scattering intensity. Thus, bead motion, $x(t)$ may referenced from an arbitrary period as long as the position within the period is fixed. For simplicity, we selected the reference position as the nearest median level of fringe intensity at the initial time. In this context, the

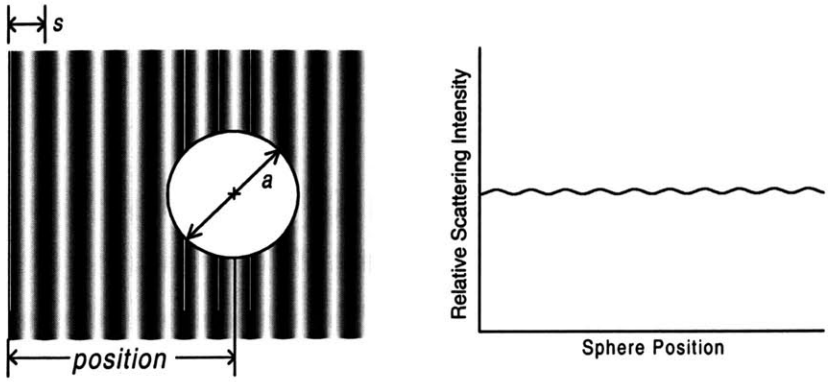

(a) Light modulation by movements of small fringes ($a = 4s$)

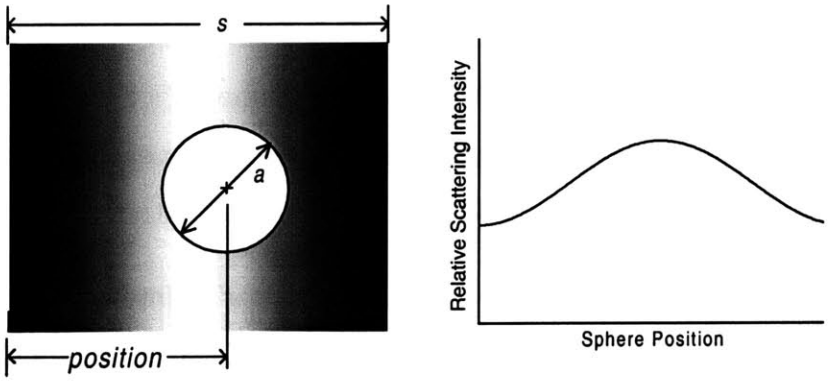

(b) Light modulation by movements of large fringes ($a = s/3$)

Figure 2-7: Relation of fringe spacing to scattering intensity. When the fringe pattern is small compared to the sphere, the modulation visibility is small (a). The peak to peak range of the AC signal is small compared to the DC offset. Since many fringes overlap the sphere, movements across fringes introduce relatively little modulation. When the fringe pattern is relatively large, the amount of reflected light changes slowly with movement (b). If the motions are constrained to a narrow range of movement, the modulation index will also be small.

scattering intensity is given by

$$I(t) = I_0[1 + V \sin(2\pi x(t)/s)] \tag{2.5}$$

where I_0 is the detected signal power from the reference position, V is the modulation visibility, $x(t)$ is the particle position, and s is the period between two consecutive fringe maxima[6].

Notice that the relation between position $x(t)$ and intensity $I(t)$ in Equation 2.5 is nonlinear. One way to characterize the amount of information available in $I(t)$ about $x(t)$ is to compute the modulation index. The modulation index is the maximum amount of phase change due to motion. From Equation 2.5, the modulation index is

$$\Delta\Phi = 2\pi \frac{\max|x(t) - x(0)|}{s}. \tag{2.6}$$

When the fringes are stationary, the variation in scattering intensity changes with the particle's initial position. Since the sinusoidal illumination pattern changes more slowly near extrema than between extrema, particle movement near an extrema will cause less variation than if it were farther away from an extrema.

Quantitatively, the percentage fluctuation in scattering intensity due to motion, γ, for a given modulation index and initial position is defined as the difference between the maximum and minimum scattering intensity divided by the scattering intensity at the initial position. To demonstrate the effects of initial position, we consider a range of motion such that the scattering intensity is monotonic with position. For these modulation indices,

$$\gamma_{DC} = \frac{|[1 + V \sin(2\pi x_0/s + \Delta\Phi)] - [1 + V \sin(2\pi x_0/s - \Delta\Phi)]|}{1 + V \sin(2\pi x_0/s)} \tag{2.7}$$

$$= \frac{2V|\sin(\Delta\Phi)\cos(2\pi x_0/s)|}{1 + V \sin(2\pi x_0/s)} \tag{2.8}$$

where γ_{DC} is the maximum percentage intensity fluctuation with a stationary fringe pattern and x_0 is the initial sphere position. Since the range of intensity fluctuation

depends on the relative positions of the sphere and fringes, the ability to determine sphere position will also depend on the initial positions. Intuitively, this is undesirable because controlled placement of the sphere is extremely difficult. Furthermore, the frequency spectrum of the signal would overlap the spectra of common, low frequency noise sources such as changes in background illumination and secondary scattered light. The signal and noise would be hard to disambiguate because their frequency spectra would be similar.

One way to combat these problems is to roll the fringe pattern at a uniform velocity. We generalize Equation 2.5 to include a phase change due to rolling fringe motion, and the resulting scattering intensity is the motion signal phase modulated onto a carrier wave at the frequency of fringe oscillation,

$$I(t) = I_0[1 + V\sin(2\pi f_c t + 2\pi x(t)/s)] \tag{2.9}$$

where f_c is the frequency of fringe oscillation as well as the carrier frequency of the motion signal[6]. The time average of the percentage fluctuation in scattering intensity becomes

$$\overline{\gamma_{FM}} = \frac{\overline{|[1 + V\sin(2\pi f_c t + 2\pi x_0/s + \Delta\Phi)] - [1 + V\sin(2\pi f_c t + 2\pi x_0/s - \Delta\Phi)]|}}{1 + V\sin(2\pi f_c t + 2\pi x_0/s)} \tag{2.10}$$

Observe that the right hand side is periodic with period f_c^{-1}, so the time average may be computed with one period. An analytic solution may obtained by applying two change of variable operations, $u = 2\pi f_c t + 2\pi x_0/s$ and $p = 1 + V\sin(u)$, and utilizing the physical constraint that the visibility, V, is in the range of 0 to 1. Applying trigonometric substitution and integrating yields,

$$\overline{\gamma_{FM}} = \frac{1}{2\pi}\int_{u=0}^{2\pi} \frac{|[1 + V\sin(u + \Delta\Phi)] - [1 + V\sin(u - \Delta\Phi)]|}{1 + V\sin(u)}\, du \tag{2.11}$$

$$= \frac{|\sin(\Delta\Phi)|}{2\pi}\int_{u=0}^{2\pi} \frac{2V|\cos(u)|}{1 + V\sin(u)}\, du \tag{2.12}$$

$$= \frac{|\sin(\Delta\Phi)|}{\pi}\left[\int_{u=0}^{\pi/2} \frac{1}{p}\, dp - \int_{u=\pi/2}^{\frac{3\pi}{2}} \frac{1}{p}\, dp + \int_{u=\frac{3\pi}{2}}^{2\pi} \frac{1}{p}\, dp\right] \tag{2.13}$$

$$= \frac{2|\sin(\Delta\Phi)|}{\pi} \ln \frac{1+V}{1-V}. \tag{2.14}$$

The motion of the illumination pattern decouples the time average scattering intensity fluctuation from the initial position. Equation 2.14 shows that the mean percentage fluctuation given visibility is the average of the percentage fluctuation given the same visibility over all initial positions. Under these conditions, position may be determined with no dependence on absolute fringe position. Furthermore, since the signal is modulated up to a higher frequency, a high pass filter may be used to remove low frequency noise without affecting signal content.

Modulating the motion signal by a fringe movement does not lose information content as long as aliasing does not occur. Each frequency component of the motion signal, $x(t)$, produces a series of side-bands around the carrier frequency in the Fourier transform of $I(t)$. These side-bands rapidly decrease outside

$$\Delta F_{sideband} = \Delta\Phi f_{sideband} \tag{2.15}$$

where $f_{sideband}$ is a specific frequency component of the motion signal. Low motion frequencies are represented by compact side-bands around the carrier while high frequencies are more spread out[11]. Thus, if the motion signal may be assumed to be frequency limited to f_{max}, the carrier frequency must be significantly greater than $\Delta\Phi f_{max}$ to avoid aliasing.

2.2.3 Effective Modulation Index

When investigating the performance characteristics of the system, the change in optical power scattered from two different positions of interest is an important consideration. If the change is small, then only a small amount of noise can be tolerated while maintaining the ability to distinguish between the two positions. Conversely, a larger amount of noise can be tolerated if the positions are farther apart.

A quantitative measurement, the effective modulation index, is created to characterize this behavior. It is defined as the average signal power for a given change in

position divided by the overall average power. By substituting Equation 2.9 into this definition, an expression for effective modulation index is found to be

$$\frac{\overline{|I(\overline{x}+\Delta)-I(\overline{x})|}}{\overline{I(\overline{x})}} = \frac{\overline{|I_0[1+V\sin(\frac{2\pi(\overline{x}+\Delta x)}{s}+\phi_0)]-I_0[1+V\sin(\frac{2\pi\overline{x}}{s}+\phi_0)]|}}{\overline{I(\overline{x})}} \quad (2.16)$$

where $\overline{x}$ represents the time average of $x(t)$, and Δx is an arbitrary small displacement of interest. By inspection of Equation 2.9, the average power is I_0. Through trigonometric expansion and small angle approximations for $\frac{\Delta x}{s}$, Equation 2.16 simplifies to

$$\frac{\overline{|I(x+\Delta x)-I(x)|}}{I_0} = \overline{|\frac{2V\pi\Delta x}{s}\cos(\frac{2\pi x}{s}+\phi_0)|}. \quad (2.17)$$

By substituting the position average of $|\cos(\frac{2\pi x}{s}+\phi_0)|$ with $2/\pi$ and substituting Equation 2.4, the effective modulation index is found to be

$$\frac{\overline{|I(x+\Delta x)-I(x)|}}{I_0} = \frac{8}{\pi}|J_1(\frac{\pi a}{s})\frac{\Delta x}{a}|. \quad (2.18)$$

It is interesting to note that the effective modulation index depends on only two dimensionless parameters: the ratio of the target diameter to fringe size and the ratio of the position change of interest to the sphere diameter. With Equation 2.18, we may conclude that the relative change in power given a position change increases linearly with the percentage of the diameter moved. Furthermore, it generally decreases as the sphere grows large compared to the fringe spacing, but it passes through an infinite series of progressively decreasing maxima.

2.3 Detection Process

Generally, target spheres are very small, and only a few nanoWatts of scattered power can be collected (Figure 2-8). A photomultiplier tube is used because of its extremely high gain. A low noise amplifier amplifies the detected light signal. Finally, the signal is low-pass filtered and is captured by an analog-to-digital capture board. The data are stored on a computer and processed off-line.

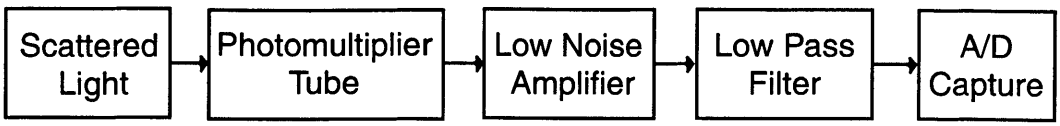

Figure 2-8: The detection process.

2.3.1 Photomultipliers

A photomultiplier tube (PMT) is a sensitive device used to measure optical radiation. The device consists of an evacuated cylinder containing a photoelectric cathode, a series of intermediate electrodes (dynodes), and an anode. When light enters through the aperture, it is absorbed by the cathode. This radiation excites electrons from the cathode's surface. These electrons are focused and accelerated through a potential field toward the first dynode. At the dynode, multiple electrons are emitted for each one that is absorbed. The electrons cascade through increasing dynode potentials and amplify the signal current. The anode collects the output power from the dynodes and drives an external load[4].

2.3.2 Noise Mechanisms

The output of a PMT is never perfectly proportional to the incident light due to noise factors. The optical power and dynode currents are carried by discrete carriers, each of whose behavior is governed by a random process. The variations in currents that this randomness introduces are called shot noise. The ratio of shot noise to signal rapidly decreases as the current becomes large because the variance of the mean of a number of independent events decreases with the number of events. Since far fewer carriers pass through the cathode than the dynodes, the cathode shot noise dominates the other sources of shot noise[4].

The current in the cathode is due to photon absorption as well as dark current. Dark current is present in the absence of illumination and is due to thermal noise and external radiation. The noise power observed at the output due to shot noise at the

cathode is

$$\overline{i_{N_1}^2} = G^2 2e(\bar{i}_c + i_d)\Delta\nu \tag{2.19}$$

where G is the total PMT current gain, $\bar{i}_c$ is the signal current at the cathode, i_d is the dark current, and $\Delta\nu$ is the observation bandwidth[4]. The rms noise density is found to be

$$\sqrt{\frac{\overline{i_{N_1}^2}}{\Delta\nu}} = G\sqrt{2e(\bar{i}_c + i_d)}. \tag{2.20}$$

Another type of noise affects PMT operation because the anode current drives a load. The random motion of carriers in the conductor introduce Johnson (thermal) noise in the output signal. The observed Johnson noise power is

$$\overline{i_{N_2}^2} = \frac{4kT\Delta\nu}{R} \tag{2.21}$$

where T is the temperature and R is resistance of the external load[4].

2.3.3 Direct Detection

In direct detection, the incident optical power is the desired signal. The PMT produces a signal current that is proportional to the incident optical power. Incident photons on the cathode stimulate electron emission. The quantum efficiency of the material is the average number of electrons emitted per absorbed photon. Consider the case where the time-average intensity of incident light is a raised, modulated cosine. The electric field incident on the detector is

$$e_s(t) = E_s[1 + V\cos(w_m t)]\cos(2\pi v_s t) \tag{2.22}$$

where E_s is the average electric field, V is the degree of amplitude modulation, w_m is frequency of the modulation, and v_s is the frequency of the incident light[4]. The photocathode current is given by

$$i_c(t) = \frac{Pe\eta}{hv_s}[1 + V\cos(w_m t)]^2 \tag{2.23}$$

$$= \frac{Pe\eta}{hv_s}[(1+\frac{V^2}{2}) + 2V\cos(w_m t) + \frac{V^2}{2}\cos(2w_m t)] \tag{2.24}$$

where P is the mean optical power incident on the cathode, η is the cathode quantum efficiency, h is Plank's constant, and e is the charge of an electron[4].

The combination of a signal AC frequency on a DC carrier yields three current frequencies at the detector: a DC component, an AC component at the incident frequency, and an AC component at twice the incident frequency. If the frequency range of incident signals is sufficiently band-limited, the undesired high frequency signals may be filtered out. If a PMT has an overall current gain of G, then the signal component of the output current will be

$$i_s(t) = Gi_c(t). \tag{2.25}$$

The output of a PMT may be viewed as an equivalent circuit where the signal and noise sources appear as parallel current sources. Since the dynode shot noise is much less than the cathode shot noise, it may be neglected without significant error. Combining equations 2.19, 2.21 and 2.25 yields an overall signal to noise ratio at the incident frequency, w_m, of

$$\frac{S}{N} = \frac{\overline{i_s^2}}{\overline{i_{N_1}^2} + \overline{i_{N_2}^2}} = \frac{G^2 2V^2(Pe\eta/hv_s)^2}{G^2 2e(\bar{i}_c + i_d)\Delta\nu + 4kT\Delta\nu/R}. \tag{2.26}$$

Since the gains of PMT's are typically extremely large, the cathode shot noise dominates the thermal noise for ordinary temperatures and resistances. In the limiting case, the signal to noise ratio reduces to

$$\frac{S}{N} \approx \frac{V^2(Pe\eta/hv_s)^2}{e(\overline{Pe\eta/hv_s} + i_d)\Delta\nu}. \tag{2.27}$$

2.4 Noise Considerations

The primary sources of noise in the system are the photomultiplier and amplifier. Other electronic noise sources, such as thermal noise, analog-to-digital conversion

noise, and external EM interference are generally much smaller than the detection noise. Optical sources of noise, such as external light sources, stray radiation, and unwanted reflections, are minimized through a carefully controlled environment and the use of modulation techniques to reduce the influence of low frequency effects. The noise sources are generally white.

An estimate of the effects of noise can be obtained by analyzing the case of amplitude modulation. The smallest possible change in position that could be determined is where the change in power due to the position change is equal to that of the noise. Since the photomultiplier shot noise typically dominates the system noise, the minimum detectable change may be found by analyzing the cathode noise. The noise current in the cathode is representative of the total amount of noise in the system. Additionally, the signal current at the cathode is the amount of detected power. As previously discussed, the effective modulation index of the system is the relative amount of the detected power that represents a small change in position. Setting the noise current (Equation 2.19) equal to the detected signal current (Equation 2.25) times the effective modulation index (Equation 2.18) yields

$$\sqrt{2e(\overline{i_c} + i_d)\Delta\nu} = \overline{i_c}\frac{8}{\pi}|J_1(\frac{\pi a}{s})\frac{\Delta x}{a}| \tag{2.28}$$

where i_c is the required signal current in the cathode to be able to detect a change of Δx in position. Typically, the required signal current is much greater than the dark current, so the i_d term may be ignored. Squaring both sides and solving for the required signal current results in

$$\overline{i_c} = \frac{\pi^2 e\Delta\nu}{32[J_1(\frac{\pi a}{s})\frac{\Delta x}{a}]^2}. \tag{2.29}$$

The amount of detected power depends linearly on the observation bandwidth and inversely with the square of the required detectable percentage change in position. The amount of collected light by the cathode is linearly related to the cathode current either by the photomultiplier's cathode radiant sensitivity specification or by Equation 2.24.

As the amount of detected light increases, the photomultiplier's relative noise strength decreases. Therefore, it is important to double check that the amplifier noise and analog-to-digital conversion noise are dominated by the photomultiplier noise. If this assumption does not hold, the representative noise power used in Equation 2.28 must be adjusted accordingly.

Chapter 3

Application Model

This research describes a scalable detection system that can be adapted to a variety of spatial and temporal resolutions. One area of active research where this would be especially helpful is in the study of the tectorial membrane — a key component of hearing systems. Spherical beads may be unobtrusively attached to the membrane, and the system is optically transparent, so interferometric methods are well suited.

3.1 The Process of Hearing

The process of hearing involves converting acoustic waves from the environment into neural signals for the brain. Humans are sensitive to sound vibrations between approximately 20 and 20,000 Hz. In most mammals, the external ear flap, the pinna, collects and directs acoustical waves into the ear canal. The waves travel down through the canal until they reach the tympanic membrane. This membrane is a taught conical structure that separates the external ear from the middle ear.

The middle ear is an air filled cavity that is connected to the respiratory system by the Eustachian tube. Two membranes, the round window and the oval window, separate the middle ear from the inner ear. Three middle ear bones (the malleus, incus, and stapes) act as levers to transmit vibrations from the tympanic membrane to the inner ear. The malleus is connected to the tympanic membrane while the stapes is connected to the oval window[12].

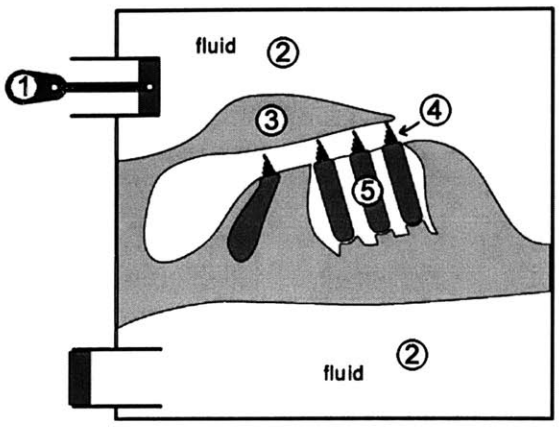

Figure 3-1: Lever model of the inner ear. The last of the middle ear bones, the stapes (1), transmits pressure waves to two fluid-filled cavities (2). These waves induce motion in the tectorial membrane (3) and embedded hair bundles (4). The relative motion of the hair bundles allows the sensory cells (5) to detect sound (Freeman [13])

The oval window and round window adjoin opposite apertures of the cochlea. The cochlea is a complex coiled structure that is filled with fluid. Essentially, the cochlea functions as a folded tube (the cochlear duct) with its top half (the scala vestibuli) connected to the oval window and its bottom half (the scala tympani) connected to the round window. A thin gelatinous membrane, the tectorial membrane, rests inside on a bed of sensory cells, the hair cells that rest on the basilar membrane.

As the stapes pushes and pulls on the oval window, pressure waves are transferred to the scala vestibuli, through the organ of Corti, and down the scala tympani to cause opposite motion in the round window. The tectorial membrane and basilar membrane vibrate relative to each other and the motion stimulates the hair cells.

Despite its prominent position in the system that transforms sound into mechanical motions of sensory receptor cells, little is known about the mechanics of the tectorial membrane. This is due at least in part to the intrinsic difficulty in experimentally testing the tectorial membrane. It is small, fragile, and transparent - which makes it a difficult target of study. Nevertheless, measuring the material properties of the tectorial membrane is important for understanding cochlear mechanics.

3.2 Determing Material Properties

A gel is essentially a mesh of macromolecules that retains vast amounts of water and ions. The tectorial membrane is a gel that is approximately 97 percent water and three percent proteins and carbohydrates. When one pushes on the gel, the proteins are forced to distort from their rest positions. In effect, they act as a network of elastic springs. This model is valid as long as the forces on the gel are slow enough that the displacement of elastic springs can follow the forces.

When the motions are very fast, the elastic spring forces exerted by the proteins are much smaller than the dampening viscous forces exerted by the water molecules and ions trapped within the gel. Since audible vibrations vary from 20 Hz to 20 kHz, these viscous properties may play an important role in process of transferring vibrational energy to the hair cells.

There have been several investigations of the stiffness of the tectorial membrane. Abnet and Freeman developed a method of embedding a magnetic bead in the tectorial membrane and pushing on it with an electromagnet[8]. With this method, they measured the stiffness of a mouse tectorial membrane to be approximately 0.2 N/m for a 10 μm bead[8]. Yet the direct approach of pushing and watching can require motions that are much larger than those during normal hearing. One way to get around this problem is to not push at all.

Because of thermal energy present in any system, molecules and particles are in constant motion. In the gel structure, bond forces constrain this motion, but over small ranges, particles are still moving randomly about. This motion is called Brownian motion and is the driving force behind diffusion.

In the range where viscous forces dominate, the thermal energy of the system will cause a uniformly random amount of movement during a small time interval. Since viscous forces dampen velocity and do not depend on position, each particle will have a higher probability of moving farther from some initial position as the time interval increases. Yet, this drifting behavior cannot go on forever in a gel. Once a particle drifts a certain distance, the spring forces will be greater than the forces due

to the thermal bouncing of molecules. The motion of a particle will be constrained to a certain range over long periods of observation. Thus, the stiffness properties can be determined with accurate measurements of the range and variation of randomly driven motion of beads.

3.2.1 Modeling Brownian Motion

A spherical particle embedded in a gel may be modeled as a bead connected to an elastic spring network immersed in a viscous medium. The average energy of the sphere is its thermal energy,

$$TE = \frac{1}{2}kT \tag{3.1}$$

where k is Boltzman's constant and T is the temperature. At a neutral spring position (with no elastic forces), this manifests as kinetic energy. As the sphere moves in the elastic medium, it transfers kinetic energy to potential energy. The potential energy stored as elastic energy by the sphere position is

$$PE = \frac{1}{2}\mathrm{Kx}^2 \tag{3.2}$$

where K is the elastic spring constant of the system and x is the deviation from a rest position.

The maximum average range of motion of the sphere will occur approximately where the average kinetic energy has been transferred to the elastic network. At this characteristic point, the elastic forces will dominate and the sphere will not move any farther from its rest position. Combining equations 3.2 and 3.1 yields a characteristic distance of

$$x_{1/2} = \sqrt{\frac{kT}{\mathrm{K}}}. \tag{3.3}$$

The characteristic distance is approximately the average maximum distance that a sphere will travel under only the influence of thermal energy.

Sphere movement during Brownian motion is a random processes. A characteristic amount of time for a sphere to move may be thought of as the amount of time that a

particle will travel a certain distance with probability one half. Under the assumption of only viscous forces, the sphere movement is driven by diffusion. The diffusibility of a sphere in a viscous medium governs how fast the sphere moves and is found by

$$D = \frac{kT}{6\pi a \eta_{visc}} \tag{3.4}$$

where η_{visc} is the viscosity of the medium and a is the diameter of the sphere[14]. The viscosity of the gel is an unknown material property. Under diffusion, the probability distribution of a sphere is a time varying Gaussian[14],

$$p(x,t) = \frac{1}{\sqrt{4\pi Dt}} \exp\left(-x^2/4Dt\right). \tag{3.5}$$

The probability distribution may be interpreted as the probability that a sphere will move a distance, x, in a time period, t. The time period serves as a characteristic time scale for each bead size and range of movement. Approximately solving Equation 3.5 for the time it would take to move a characteristic distance, $x_{1/2}$, with probability one half yields[14]

$$t_{1/2} = \frac{x_{1/2}^2}{D}. \tag{3.6}$$

3.2.2 Modeled Range of Movement

For the purposes of estimating the range of motion of a bead connected to a spring network, the spring constant was estimated by assuming that it scales linearly with sphere diameter[15]. The reported stiffness of 0.2 N/m for a 10 μm diameter bead was linearly interpolated for each modeled bead size[8]. The viscosity of the surrounding medium was unknown. Since a gel is primarily water, for purposes of estimating characteristic times and distances it was estimated by assuming that the gel had approximately the same viscosity as water. The diffusibility for each bead size was estimated with these parameters from Equation 3.4.

The characteristic distance scales inversely with the square root of bead diameter because the estimated spring constant (Equation 3.2) linearly increases with bead

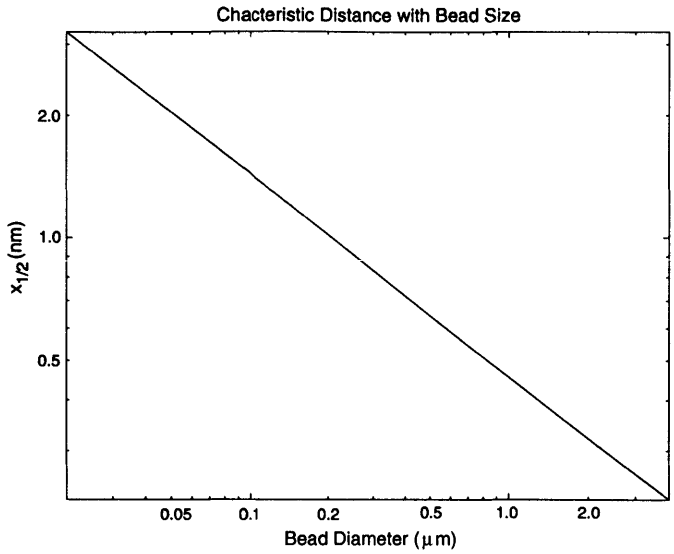

Figure 3-2: Approximate range of bead movement at room temperature.

diameter. From Equation 3.3 the characteristic distance for a 0.1 μm diameter sphere was found to be approximately 1.4 nm, while the characteristic distance of a 1 μm diameter sphere was found to be 0.5 nm (Figure 3-2).

From Equation 3.6, the characteristic time depends on the square of characteristic distance, which scales inversely with diameter, divided by the diffusivity, which also scales inversely with diameter. Thus, the mode of characteristic time shows no net dependence on bead size. The characteristic time for this model was found to be approximately 0.4 μs.

3.3 Modeling a Detection System

The idealized fringe based motion detector consisted of an illuminator, a detector, and a signal processor.

3.3.1 Target Illumination

We modeled the illumination system as two beams that intersect near their waists. Each beam had a wavelength (λ_1 and λ_2) and a power. It was assumed that the

beams path lengths differ by less than the coherence length and polarized in the same direction so that interference occurs. Both beams were assumed to be of the same power. The projection of the fringe volume onto the observation plane was modeled by a fringe period, spot size, and power density. The scattering object was simplified as a sphere with a diameter and an index of refraction.

The fringe periods were determined by the angle of beam separation. Diffraction limits constrained the minimum fringe period. Geometric constraints that govern the ability to deliver narrowly spaced beams determined the maximum fringe period.

The light scattered by the bead was modeled by Mie scattering. The measured intensity of scattered light was determined by the relative size of the bead to the wavelength of light, the index of refraction, and the angle of observation (Figure 2-6).

3.3.2 Detection System

Light collection was modeled as an ideal lens collector followed by a photomultiplier. It was assumed that the target was in the image plane of the lens. It was further assumed that the target was the only scattering particle in the field of view of the lens. The lens observed a cone of scattered light with diameter proportional to its numerical aperture. The photomultiplier was characterized by its cathode efficiency, dark current, and gain.

3.3.3 Signal Processing

In this system model, it was assumed that limiting noise factor would be from the shot noise at the photomultiplier cathode. To estimate the required operating parameters, other optical and electronic noise factors were neglected.

3.3.4 Modeled Results

The characteristic distance was computed for a range of bead diameters from 200 nm to 4 um (Equation 3.3). For each diameter, the fringe period was found by maximizing the effective modulation index the feasible fringe periods (Equation 2.18).

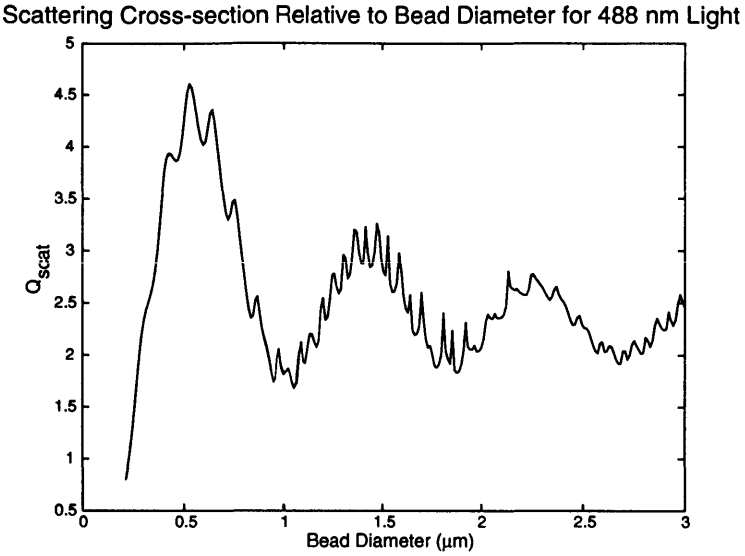

Figure 3-3: Ratio of scattering cross-section to geometric cross section. The index of refraction of the modeled beads was 1.59. The broad sequence of extrema, known as the interference structure, can be considered to be interference due to path length differences between rays traversing the sphere[16]. The irregular fine oscillations, known as the ripple structure, are due to electromagnetic resonances of the sphere[16]. For more strongly absorbing spheres, both oscillation structures are dampened.

The scattering function and cross-section were calculated with the Mie Scattering Toolbox (Figure 3-3). Note that the scattering cross-section may be larger that the geometric cross-section because the target interacts with the light and effectively bends the light so that more radiation interacts with the geometric cross-section than would pass through a region of the same size in the absence of the target. The scattering functions were numerically integrated over the cone of observation of 0.5 NA lens tilted at 85 degrees from the incident radiation. For bead diameters larger than 0.5 micrometers, the 0.5 NA lens collects 0.2 to 0.5 percent of the light scattered by the sphere (Figure 3-4). Approximately 1 percent of the scattered light is collected for 0.5 micrometer diameter beads.

The resolution for each bead diameter and fringe period was computed by solving for the change in bead position that would result in a change in cathode current (Equation 2.24) equal to the rms noise at the cathode (Equation 2.19). Figure 3-5

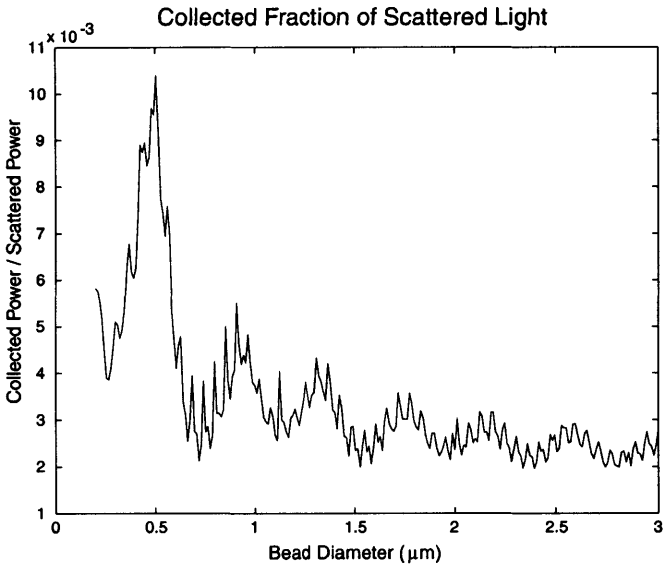

Figure 3-4: Modeled collected fraction of scattered light. When a 0.5 NA lens is used to collect scattered light at an angle 15 degrees off back-scattering, approximately 1 percent of scattered light is collected for 0.5 micrometer diameter beads. The fraction of collected light rapidly decreases to several thousandths for other bead diameters and generally decreases with bead size.

shows the resolution is inversely proportional to the square root of the power density and nearly constant across bead diameters from 100 nm to 3 μm.[1] The resolution has a minima with 0.5 μm spheres and is nearly constant for spheres larger than 1 μm.

The dependence of the overall resolution on the observation bandwidth is straightforward. Noise power (modeled as a white source) increases with the square root of observation bandwidth. Given a bead, fringes, and illumination, the resolution scales inversely with noise power. Thus, the resolution scales inversely with the square root of observation bandwidth.

The intensity of light scattered by a sphere linearly increases with illumination intensity. Yet, the noise due to photon capture increases with the square root of the collected power (Equation 2.19). The resolution scales with the increase in signal to noise ratio, which scales with square root of incident power.

The dependence on bead size is more difficult to visualize since the fringe period is optimized for each bead diameter. The optimization method maximizes the effective modulation index (Equation 2.18) by maximizing the modulation visibility times the modulation index. Maximizing over feasible fringe periods results in approximately constant modulation visibility with a fringe period proportional bead diameter.

Since the modulation index depends on the change in position relative to fringe period, the modulation index is inversely proportional to bead size. As a bead become large, a constant amount of movement generates a decreasing amount of signal modulation. Yet, larger beads scatter more light and generate stronger signals. These effects roughly cancel and there is little resolution dependence on absolute bead diameter. The observed variation in resolution with bead size closely corresponds to the non-linear variations in scattering with bead size that were illustrated in Figure 3-3.

Although the absolute resolution (the ability to detect a fixed size change in position) does not depend heavily on bead size, the ability to measure Brownian motion does depend on bead size. The characteristic distance is smaller for large beads

[1]Resolution refers to the level of detected movement that is equally likely due to noise or actual change. Measurements smaller than this amount are more likely to be noise than movement, and measurements larger than this amount are more likely attributable to movement than to noise.

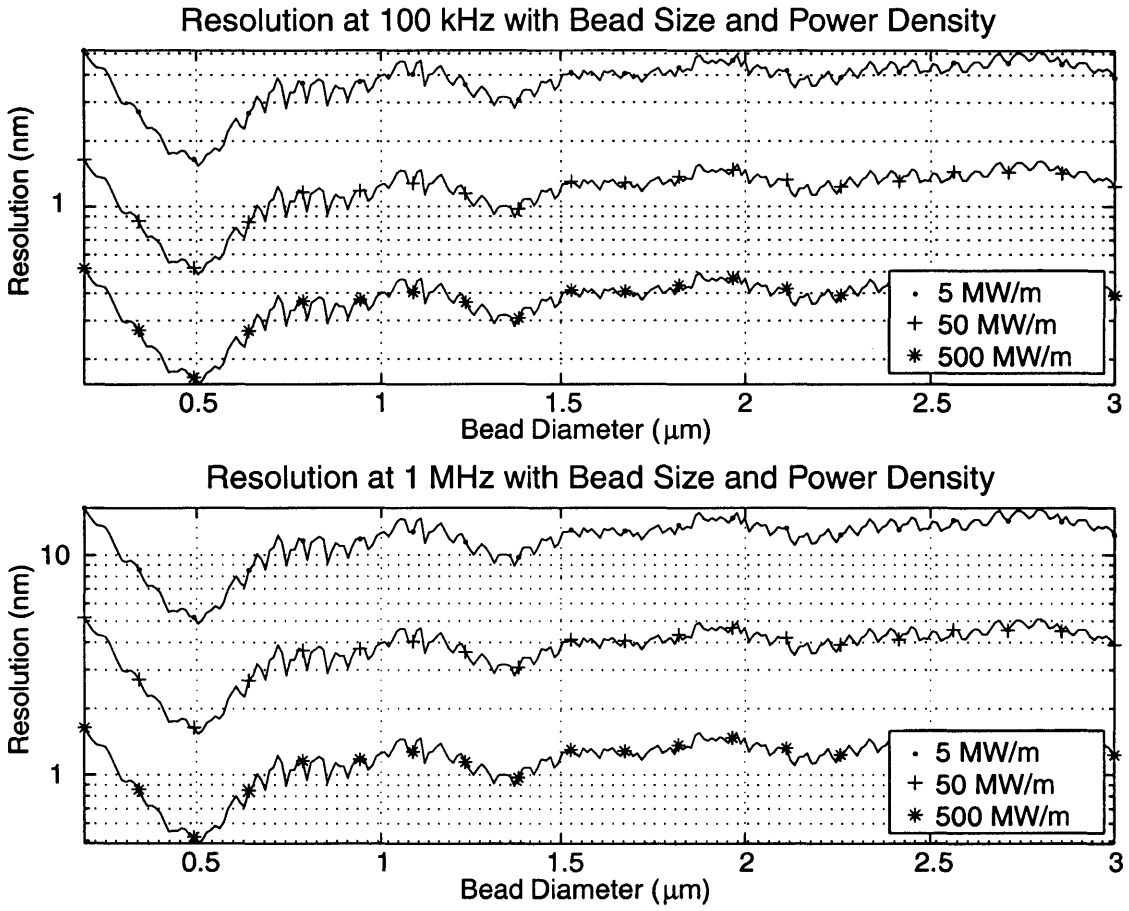

Figure 3-5: Modeled sensitivity of detection system in nanometers with latex spheres in 488 nm light.

than small beads (Figure 3-2). The systems ability characterize the Brownian motion of beads may be represented by relative resolution as the ratio of the characteristic distance to the system resolution (Figure 3-6).

As would be expected from the discussion on absolute resolution, the relative resolution increases with the square root of illumination intensity and decreases with the square root of observation bandwidth. Since the characteristic distance is inversely proportional to bead size, the signal to noise ratio decreases with bead size. The relative resolution was at a maximum for a bead diameter of 0.5 μm.

In summary, the model predicts that absolute resolution will be generally constant for a given bead diameter, but variations in scattering proprieties will give rise to ripple-like variations. The resolution scales with the square root of incident power and inversely with the square root of observation bandwidth. If the system is used to measure Brownian motion, the model predicts that 0.5 μm beads would be the most effective in characterizing the motion.

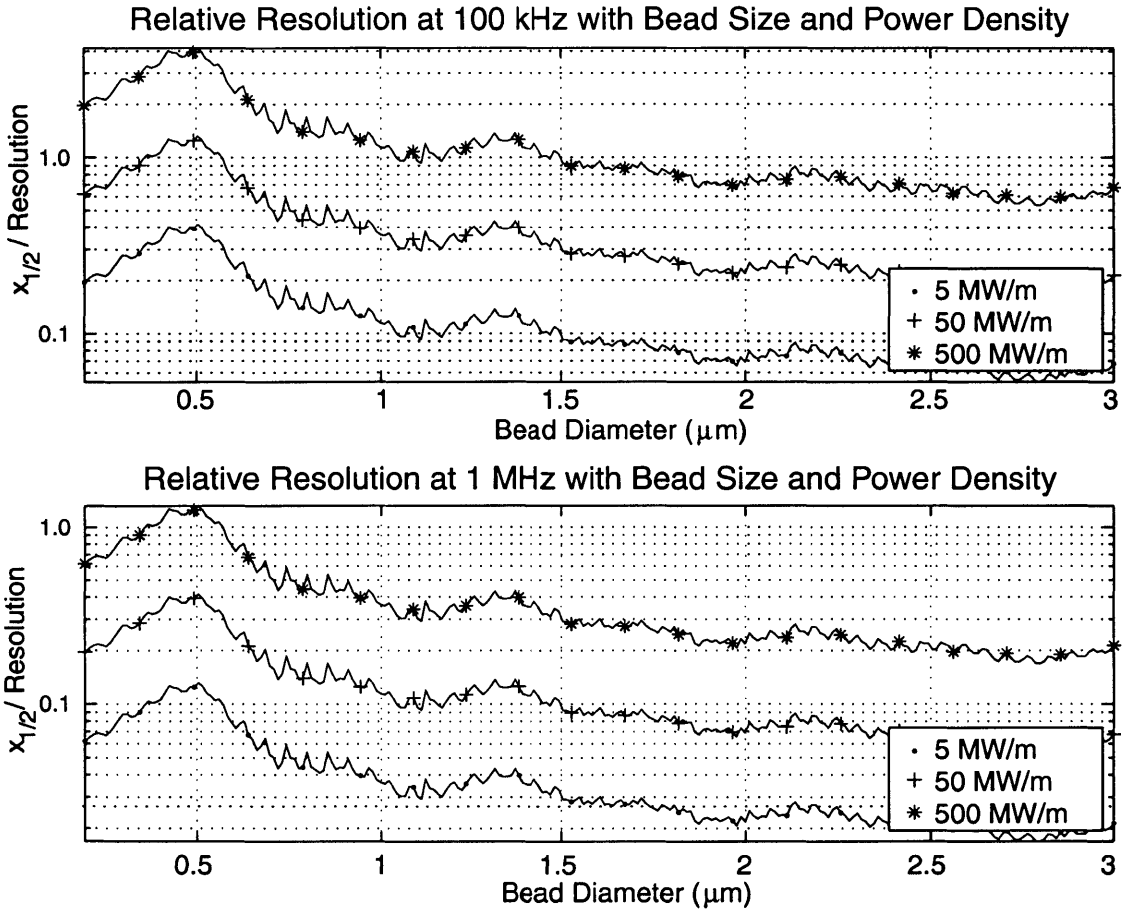

Figure 3-6: Modeled sensitivity of detection system relative to the modeled motion of a latex sphere undergoing Brownian motion with 488 nm illumination.

Chapter 4

Stationary Fringe Prototype

A stationary fringe motion detection system was developed to investigate practical implementation issues relating to measuring motion by projecting fringes and sensing scattered light. The device intersected two beams of the same frequency to form a non-rolling fringe pattern beneath an objective. A bead was then moved under piezo control across the pattern. The intensity of scattered light, modulation depth, and non-idealities were explored.

4.1 Device Overview

The prototype was constructed on one side of a large optics table with a shared beam path down the center of the table (Figure 4-1). The system projected fringes in the field of view of a modular c-mount tube microscope (Figure 4-2). The functional components of the prototype consisted of a fringe projection system, an analog signal detection system, and a digital signal processing system. The system collected phase modulated position information with a series of optical to electrical analog to digital transformations (Figure 4-3).

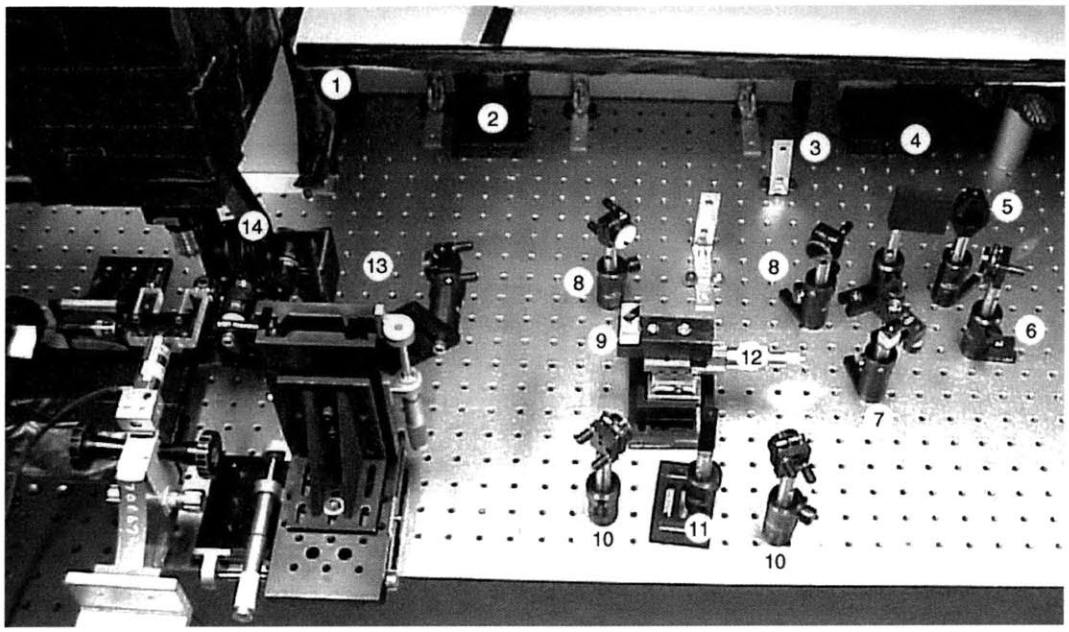

Figure 4-1: Stationary fringe projector optics layout. The primary beam (1) was first filtered by four neutral density filters of additively combined optical density 1.0 (2). The beam passed through an inactive AOM crystal (3) and was diverted by a mirror (4) toward two more ND filters of combined optical density 1.2 (5). Another mirror (6) centered the beam in a beam splitter cube (7). The reflected beam was directed toward a right angle prism (9) by two control mirrors for that beam (8). The transmitted beam was also redirected by two control mirrors (10). A 0.1 neutral density filter attenuated the transmitted beam to match the reflected beam intensity (11). The two beams emerged roughly parallel from two right angle prisms (9) that were mounted so that their hypotenuses were at a right angle. A translation stage (12) moved the prisms so that beam separation could be adjusted once alignment was complete. A series of two mirrors (13) raised the beams by approximately 10 cm and directed them into the back of an objective (14). The objective and last mirror in the beam path were mounted on a three-axis translation stage to adjust the position of the focal plane relative to the field of view of the microscope. A black foam board, located out of view to the left, served as a beam stop 30 cm from the focal plane of the objective.

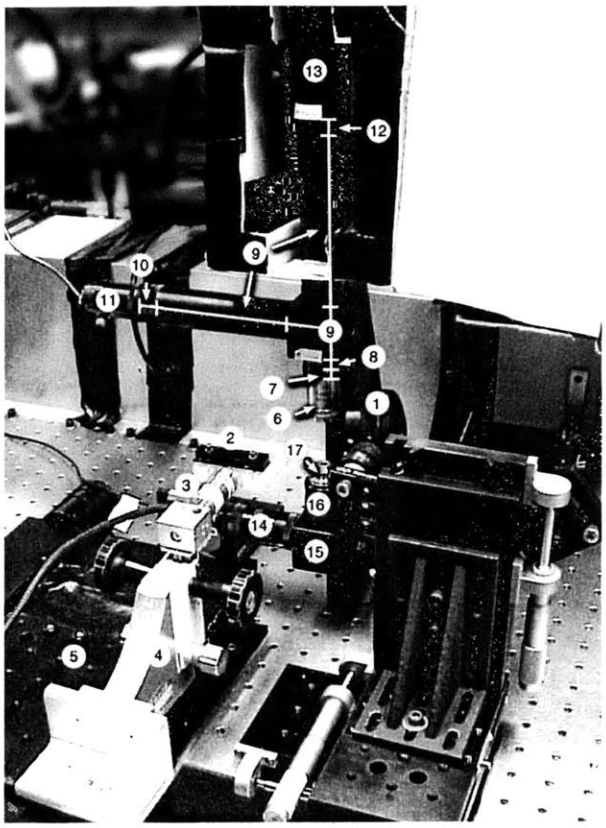

Figure 4-2: Microscope construction. Fringe patterns were projected through an objective (1) (10x Epiplan Zeiss, #442930) onto a stage (2). The stage was moved perpendicularly to the fringes by a piezo element (3) (E-515, Physik Intrumente). A three axis translation stage was constructed from a microscope arm and computer-controlled two axis stage (5). Light was collected by an objective with NA 0.5 (6) (50x Epiplan LD Zeiss, #442850) that was mounted to the scope with a 6 mm thick ring (7). A 12 mm iris (8) (NT03-623, Edmund Industrial Optics) regulated the light exiting the rear aperture of the objective. A 30R-70T beam splitting plate (9) (NT45-324, Edmund Industrial Optics) with a path length approximately 38 mm reflected 30 percent of the light down a 112 mm tube (9) and a 24 mm mounting ring (10) to a CCD camera (CVC-120R, ProVideo) in a c-mount clamp (11) (17 mm). The beam splitter transmitted 70 percent of the light down a different 112 mm tube (9) and past an identical 12 mm iris to a 5 mm mounting ring (12). A photomultiplier tube (HC124-07, Hamamatsu) was mounted in a custom c-mount adapter (13) (5 mm). The cathode was set back approximately 25 mm from the assembly aperture. The photomultiplier assembly was enclosed in a box of insulation to prevent detection of extraneous light (shown open). Transmission illumination for use during focusing was provided by a surface mount LED on a tip-tilt stage that was mounted in a c-mount tube (14). A mirror box (15) directed the light upwards down an adjustable length tube (16) to a low magnification objective (17) (3.5x Leitz Wetzlar).

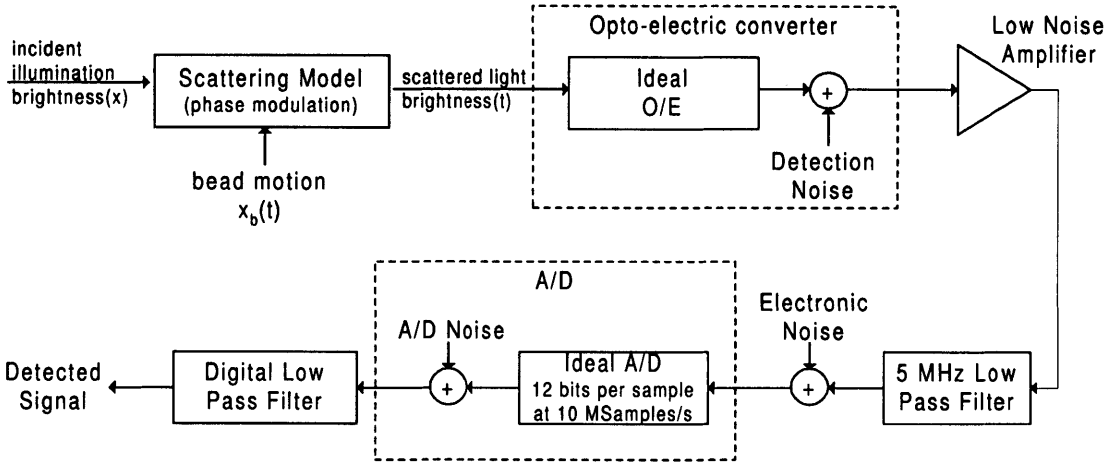

Figure 4-3: Signal processing method. The photomultiplier converted optical power into electrical current. A low noise amplifier (C6804-01, Hamamatsu) amplified the current source across a 50 ohm impedance. An 11 pole elliptical low pass filter (LP1161-5M-50-6913, TTE) band-limited the data to 5 MHz with a stop-band attenuation of -69 dB. An analog to digital capture card (PCI-417B, Datel) and a digital oscilloscope (TDS-460A, Tektronix) digitized the filtered signal. Digital signal processing was performed in Matlab (Mathworks).

4.1.1 Fringe Projection and Observation

An argon ion laser (Inova 304C, Coherent) was used because of its long coherence length and wide range of power output (as well as its ready availability). The 488 nm wavelength was selected to best approach the maximum sensitivity of the photomultiplier tube at 420 nm. The optics were designed to project micrometer sized fringes that intersected the field of view of the observation microscope (Figure 4-1).

A manual z-axis translation stage was mounted on a 2-axis computer/joystick controlled stage. A feedback stabilized piezo device was mounted on the top of the stage. A custom made Plexiglas stage was bolted to the end of the piezo stack. A rubber-lined plastic strip was bolted to the end of the Plexiglas holder. Specimen slides were slid underneath the tie down and firmly mounted to the stage. The entire assembly was bolted to a vibration dampening table.

4.1.2 Analog Signal Detection System

The photomultiplier linearly supplied current in response to incident optical power up to the saturation point of 100 μA. The optical to electrical gain was controlled by adjusting a reference voltage with a potentiometer. The internal high voltage power supply ranged between 500 and 1200 V.

The output of the photomultiplier tube was connected to a low noise amplifier. The output of the amplifier was low pass filtered at 5 MHz by an 11 pole elliptical filter with 69 dB stop-band attenuation. The filtered output was captured by an oscilloscope and a computer-controlled analog-to-digital card.

The piezo stimulus device contained an integral capacitive position sensor. To obtain simultaneous measurements of position with scattered light, the output of this sensor was buffered, scaled, and shifted by an op amp circuit (Figure 4-4). The output of this circuit was also captured by an oscilloscope and a computer-controlled A/D card.

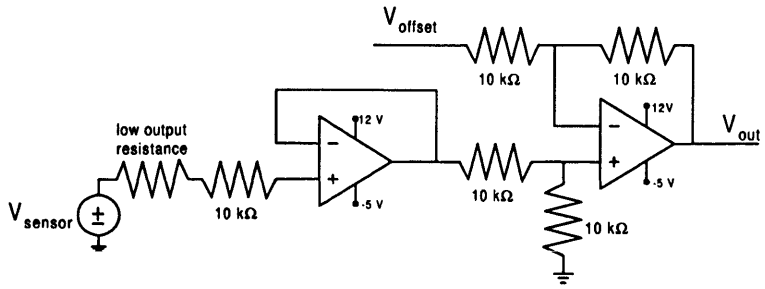

Figure 4-4: Circuit design for piezo position buffer. The left-most resistor decreased the signal voltage and the left-most op amp (AD713, Analog Devices) buffered the signal. The second op amp and four resisters acted as a subtracting circuit. V_{offset} was typically 4.1 V. The input range was 1.5 to 10.5 V and the output range was -2.5 to 1.5 V.

4.1.3 Digital Processing

Data acquisition, signal processing, and piezo position were controlled through Matlab scripts. Experiments and calibration procedures were also written as Matlab scripts. Processing was done on an Intel PIII-500 machine (XPS-T500, Dell).

The computer controlled piezo had an active range of 10 μm with nanometer stability. In "function stimulus" mode, the piezo could move to a periodic sequence of up to 1024 locations separated by 4 ms.

A custom program controlled an analog to digital capture board running in interrupt driven DMA transfer mode. It was able to capture up to 16,777,216 samples at rates between 5 and 20 megasamples/s (from two channels simultaneously). The card had a dynamic range of -2.5 to 2.5 V with 12 bits of resolution. It also supported a TTL trigger channel to synchronize data acquisition. The custom software supported on-the-fly FIR filtering and down-sampling to accelerate data transfer to Matlab.

Since the scattered light signal was low pass filtered in hardware at 5 MHz, the data were sampled at 10 megasamples/s to avoid aliasing effects. To achieve different observation bandwidths, the data were digitally filtered with 13th order Chebyshev filters applied in forward and reverse directions to achieve zero phase. The filters were generated by the Matlab decimate command.

The video output of the CCD camera was digitized by a TV tuner video card (Marvel G400-TV, Matrox). Although the video quality was less then ideal, it provided a fast and inexpensive method of monitoring bead position and modulation. Still frames were captured with the provided software.

4.2 Calibration

4.2.1 Photomultiplier Sensitivity

The photomultiplier spectral response and gain were extremely sensitive to the wavelength of light and control voltage. The photomultiplier was not pre-calibrated for 488 nm light. Since the exact quantity of light detected was not critical, manual calibration was performed.

A weak (250 nW) beam was isolated and the intensity was measured with a pre-calibrated photodiode (Fieldmaster, Coherent). The photomultiplier was allowed to dark adjust for 30 minutes. Then, for each control voltage from 0.6 to 1.2 V in 0.1 V increments, a series of neutral density filters was placed between the beam and the photomultiplier cathode. The mean voltage output after an amplifier and 5 MHz low pass filter was recorded.

In the range of calibration, the photomultiplier should have been in the linear regime, so the experimental data were fit to a linear model using least squares. The photomultiplier specifications also call for a logarithmic increase in gain with control voltage. The logarithms of slopes of responses at each power were least squares fit to a linear response (Figure 4-5). The model was

$$V_{obs} \approx P_{incident} 10^{3.20 V_{Ctrl} - 3.56} \tag{4.1}$$

where $P_{incident}$ is the incident power in nanoWatts, V_{obs} is the detected voltage, and V_{Ctrl} is the control voltage applied to the photomultiplier.

The one-third inch diagonal CCD sensor only covered a small section of the tube microscope cross section, so it was only possible to see a fraction of the light entering

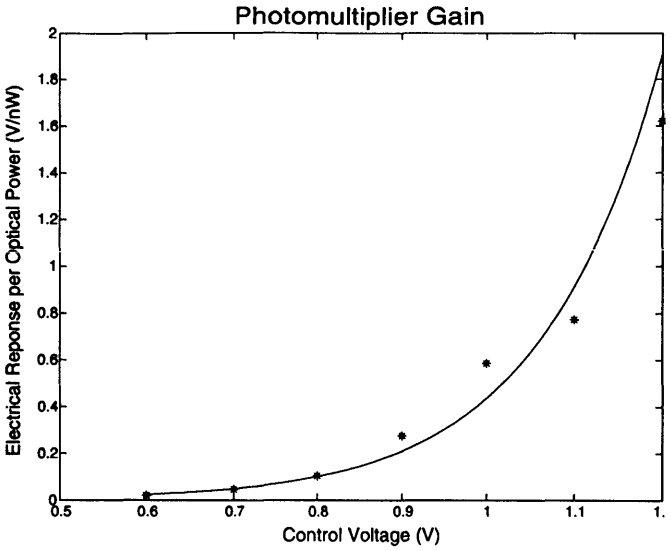

Figure 4-5: Least squares fit to photomultiplier gain. The measured gains at seven different control voltages (symbols) were fit (solid line) to an exponential function of control voltage.

the tube microscope. To prevent the photomultiplier from detecting light that was not scattered by particle of interest, an iris was placed directly before the cathode aperture. The field of view for each iris setting was determined by temporarily replacing the photomultiplier with a second CCD. The field of view was determined by comparing images taken from the two cameras. Guides were placed on the microscope monitor to aid in centering the target (Figure 4-6).

4.2.2 Detection Noise

The noise sources in the system can be broadly categorized as either generated by the system without input or generated by the system because of interaction with the input. The signal independent noise floor was measured by extinguishing all possible sources of light, closing all apertures, and minimizing photomultiplier gain. Figure 4-7 shows that the power spectral density[1] of the observed response has spikes in the megaHertz range and a slight inverse frequency component in the sub-megaHertz

[1]All power spectral density calculations were done with periodogram estimations.

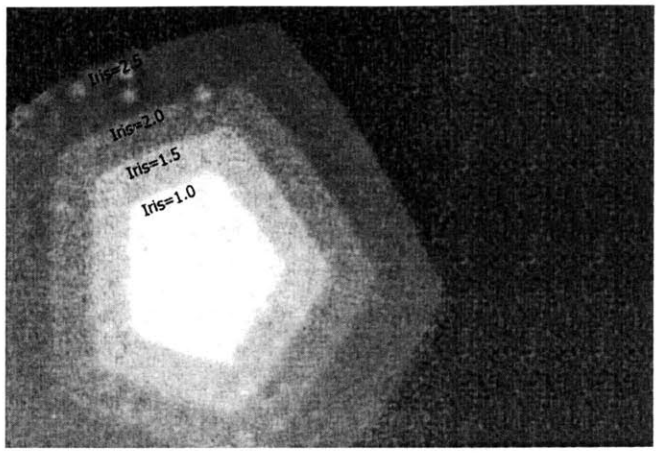

Figure 4-6: Photomultiplier field of view. The concentric pentagons show the area of the camera view that is within the photomultiplier field of view for iris settings 1.0, 1.5, 2.0, and 2.5.

range. Additionally, there was broadband white noise of approximately -110 dB/Hz. To determine the limiting noise component, the amplifier was driven with zero-current input (an open circuit) and the output was captured with the analog-to-digital card. A similar pattern of high frequency spikes and an inverse frequency component were evident in the power spectrum of the zero-current response.

To establish a noise floor for each set of experimental conditions, data were acquired while the bead was in place, but was not being stimulated. In the absence of a stimulus, no motion was assumed, so the detected motion was categorized as noise. The variance and power spectral density were used characterize the noise during motion stimulus.

4.2.3 Piezo Movement and Translation Circuits

A computer-controlled piezo was used to move the slide through the fringes. The position sensing signal offered extremely low output resistance and was out of the range of the A/D card, so it was passed through an active circuit to buffer, shift and scale the signal. The noise in the conversion circuit was analyzed by comparing the direct signal with the processed signal on an oscilloscope that had a larger dynamic

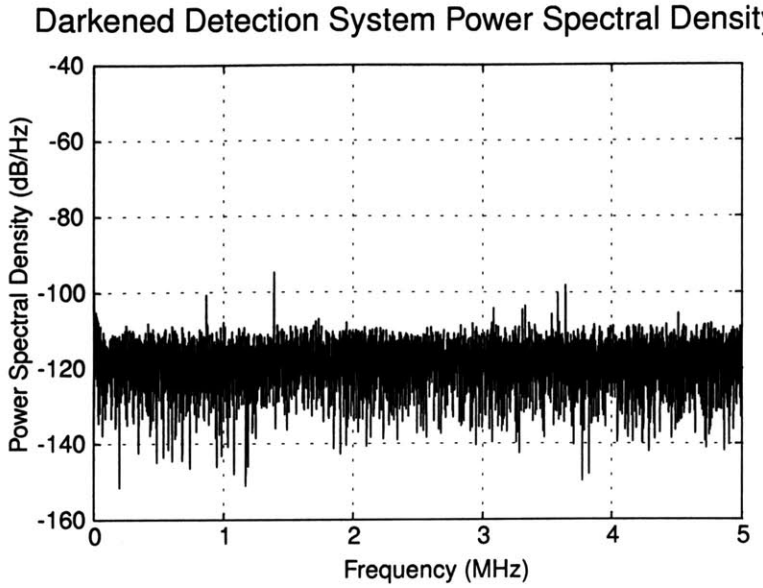

Figure 4-7: Detection system noise floor. The system output was measured with minimal light stimulation. The noise was non-white at low frequencies and exhibited several high frequency spikes. Broadband white noise of -110 dB/Hz was present.

range than the A/D card. The rms noise was found to be between -75 dB/Hz in the DC to 10 kHz range and -100 dB/Hz of broadband noise.

Initial experiments revealed that the position sensor had a significant delay relative to the motion of the target. A laser Doppler interferometer (OFV 511, PolyTech) was used to measure the position of the target. The analog-to-digital card captured 150 millisecond traces of simultaneous sensor output and laser Doppler position measurement (Figure 4-8). The signals were aligned by minimizing squared differences over time shifting, voltage scaling, and voltage offsetting. The signals were linearly interpolated to allow for fractional delays. This method found that the piezo sensor lagged behind the laser Doppler readings by 153.6 μs for the pulse train stimulus used in the experiments. The delay time was found to vary based on the command waveform.

The laser Doppler interferometer was also used to measure motion of the piezo stage in two directions orthogonal to the intended direction of motion. The sensor

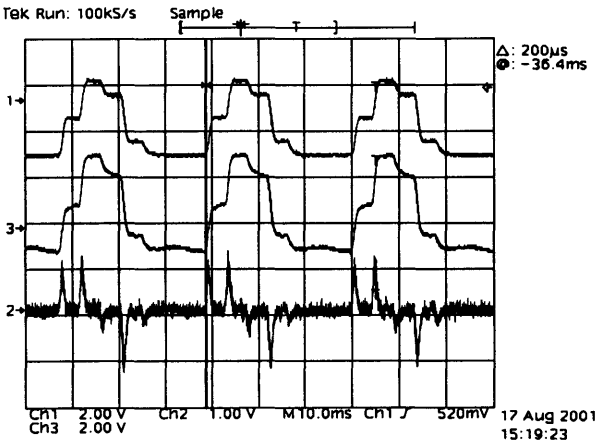

Figure 4-8: In-line piezo sensor analysis. The top trace shows the piezo capacitive sensor position reading. The middle trace shows a laser Doppler reading of the same motion. The bottom trace shows the velocity that was directly reported by the laser interferometer. A delay of 153.6 μs was found between the piezo sensor and the Doppler measurements.

was manually aligned to be perpendicular to the direction of motion. A maximum of 1.6 μm out-of-specimen-plane and in-specimen-plane movement were for a 10 μm oscillatory stimulus (Figure 4-9).

4.2.4 Target Preparation

Polystyrene microspheres were used as scattering objects. The beads were diluted in ethanol and mixed on a vibration table (Vortex Genie 2, VWR Scientific). The 1 μm (#07310, Polysciences) and 2 μm beads (#19814, Polysciences) were diluted 1:1,000 (bead solution to ethanol). The 0.24 μm (#07304, Polysciences) and 0.5 μm beads (#07307, Polysciences) were serially diluted to 1:1,000,000 (bead solution to ethanol). The solutions were sonicated with a Cole-Parmer 8850 for 5 minutes to break up clumped beads. Slides for 0.5, 1, and 2 μm beads were prepared by depositing 1 μL of solution near the end of a 25 x 75 mm slide and letting the ethanol evaporate. The 0.24 μm solution contained many impurities and isolating beads with the above method proved nearly impossible. Instead, half of a slide was flooded with 40 μL ethanol and held at a 5 degree angle. One μL of 0.24 μm beads was deposited

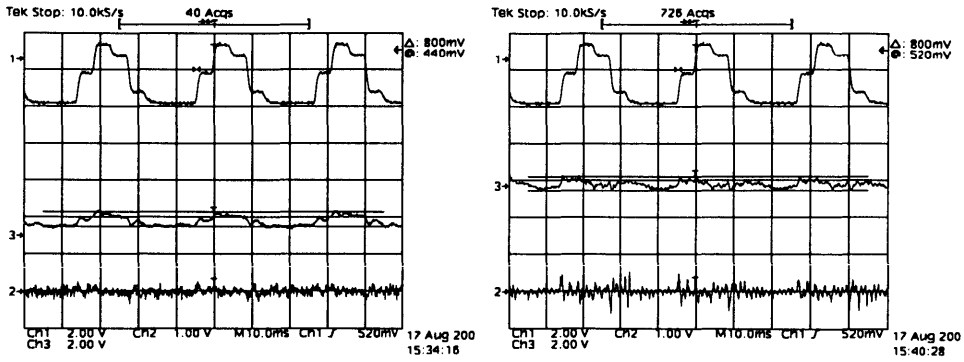

Figure 4-9: Out-of-line coupling. The piezo was swept through a 10 μm range of movement shown in top trace in both figures. The relative horizontally coupled motion is shown the left in the second trace while the vertical coupling motion is shown on right. In both cases out of plane movement was less than 1.6 μm (corresponding to 800 mV). The laser Doppler velocity readings for both positions are shown as the bottom traces.

near the top of the slope in the ethanol. The slide was left for 5 minutes as the ethanol evaporated. The particles of different sizes diffused different distances and it was possible to locate isolated beads.

Once the target slide was mounted on the slide holder in the translation stage, focus was obtained with the video output of the CCD screen. LED position was adjusted to achieved maximal uniform lighting. The iris behind the objective was stepped down to reduce unwanted glare. Slide position was adjusted until one bead was in the field of view and a minimal number of particles were visible elsewhere outside the field of view of the photomultiplier.

4.2.5 Optical Alignment

The alignment procedure for the prototype was extremely cumbersome. The mirrors were coarsely aligned so that the beams were approximately parallel entering the back of the objective. The objective was then positioned so that the focus of the projection objective visually appeared to be in the field of view of the collector objective.

Iteratively, one beam was selected and the other beam was blocked. Using the two control mirrors, the last mirror before the objective, and the objective translation

stage, the intersection of the first beam with the target was aligned to be in the field of view of the photomultiplier. Then the other beam was swept through its range of possible positions with its control mirrors. Alignment was complete when both beams intersected and their projections appeared as small as possible on the CCD.

4.3 Method

For each experiment, a bead slide was prepared and mounted. The slide was scanned until an isolated single bead of representative size could be found. When selected, the target bead was visually centered in the photomultiplier field of view. An image of the bead size and position was captured.

With the bead in place, the laser was turned on with all neutral density filters in place. Each beam was approximately 200 μW while the laser output power was 250 mW. The laser output power was typically unstable and varied 10 percent on a time scale of minutes. The beams were aligned to form fringes in the target area. The fringes for this experiment were approximately 3 μm across and had minimum cross section size of approximately 50 μm.

For each beam, one beam was blocked and the piezo was moved at 2 Hz through its range of motion. The oscilloscope trace of the intensity of light was inspected to ensure that the individual beam intensity was constant during the bead movement. Then, both beams were unblocked.

The amplifier specifications stated that it saturated at -1.5 Volts, but it was observed to exhibit non-linear behavior at slightly greater voltages. While the piezo was moving, the gain of the photomultiplier was adjusted to maximize detected voltage while remaining greater than -1.4 Volts. The effects of the changes were observed in real time with an oscilloscope.

The piezo was moved to its center position (10 μm) and held stationary. Twelve milliseconds of data were captured at 10 megasamples/s to determine the noise floor of the specific light level and photomultiplier gain setting. Then, the piezo was continuously moved through a 20 millisecond pulse through its active range (5 to 15

μm) with a 40 millisecond delay between stimuli. The piezo took 4 steps to complete the pulse and delayed approximately 4 ms at each step.

The scattering data and position data were simultaneously captured for 204.8 ms (2,048,000 samples at 10 MHz). This encompassed approximately seven complete waveforms of the stimulus. The experiment was repeated 3 times for each bead at different power levels. One experiment was run with all neutral density filters in place (approximately 400 μW incident), once with only the inner filters in place (approximately 6 mW incident), and once with no filters in place (approximately 70 mW incident).

4.4 Results

4.4.1 Modulation

To test the static fringe prototype, a piezoelectric crystal was used to move a bead through the fringe pattern and scattered light was measured. The bead was moved in a saw tooth pattern that spanned several fringes. As the bead moved linearly through the fringe pattern, the scattered brightness varied approximately sinusoidally (Figure 4-10).

Although the piezo crystal response time was sub-millisecond, new positions could only be programmed every 4 milliseconds. During experiments that operated at 100s of Hertz, the stimulus was a periodic train of rapid steps. The bead was at rest during the majority of the experiment and quickly swept through most of the range of motion during position changes. Thus, the scattered light traces interleave periods of little change with rapid sweeps through a sinusoidal pattern (Figure 4-11). The resulting data are periodic, but visually difficult to associate with sinusoidal illumination.

The modulation characteristics varied across experiments. For all but one experiment, the modulation visibility was less than the model predicted (Figure 4-12). Within each bead size, the visibility also varied. The amount of scattered light generally increased with the incident power (Figure 4-13). While the power accurately

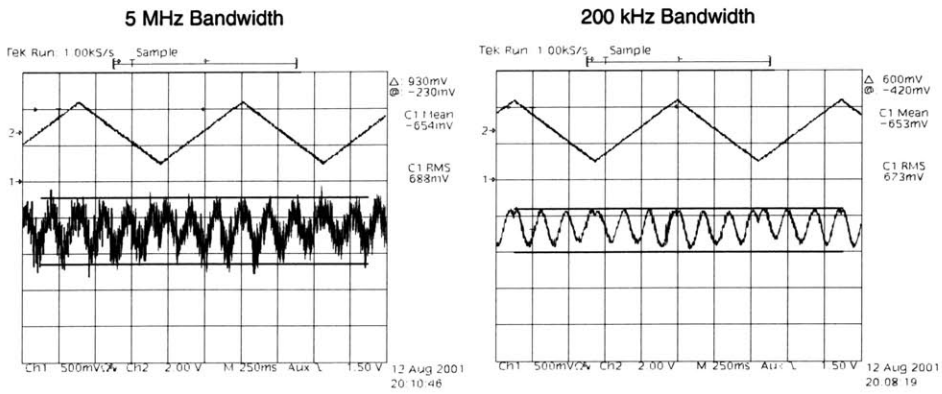

Figure 4-10: Demonstration of modulation. A 1 μm bead was linearly swept through a 10 μm range across a fringe pattern with approximately 3 μm spacing. The bead cycled at 0.9 Hz. When illuminated by a total of approximately 5 mW, modulation was evident at both 5 MHz (left) and 200 kHz (right) observation bandwidth.

measured with the PMT, the spot size could only be measured from images taken by the CCD cameras. The CCD used to monitor the experiment utilized auto-contrast and brightness adjustment so the absolute brightness of captured images was not indicative of the intensity of scattered light. The beam cross-sections were approximately Gaussian, so precisely measuring beam diameter without a two-dimensional measure of absolute intensity proved problematic.

To determine the temporal stability of the illumination pattern and explore demodulation techniques, the light intensity was plotted as a function of position. (Figure 4-14) It was found that synchronization of the piezo position with the scattered light was critical to profiling the motion intensity. Misalignments in the signals cause vertical jumps and phase misalignments in the traces of the sinusoidal fringe patterns.

4.4.2 Noise

At low levels of illumination (and corresponding high photomultiplier gains), broadband white noise dominated the signal independent noise shown in Figure 4-7. At higher power levels (and lower photomultiplier gains), the noise power spectral density began to reveal the spectrum of the detection system noise floor (Figure 4-15). A

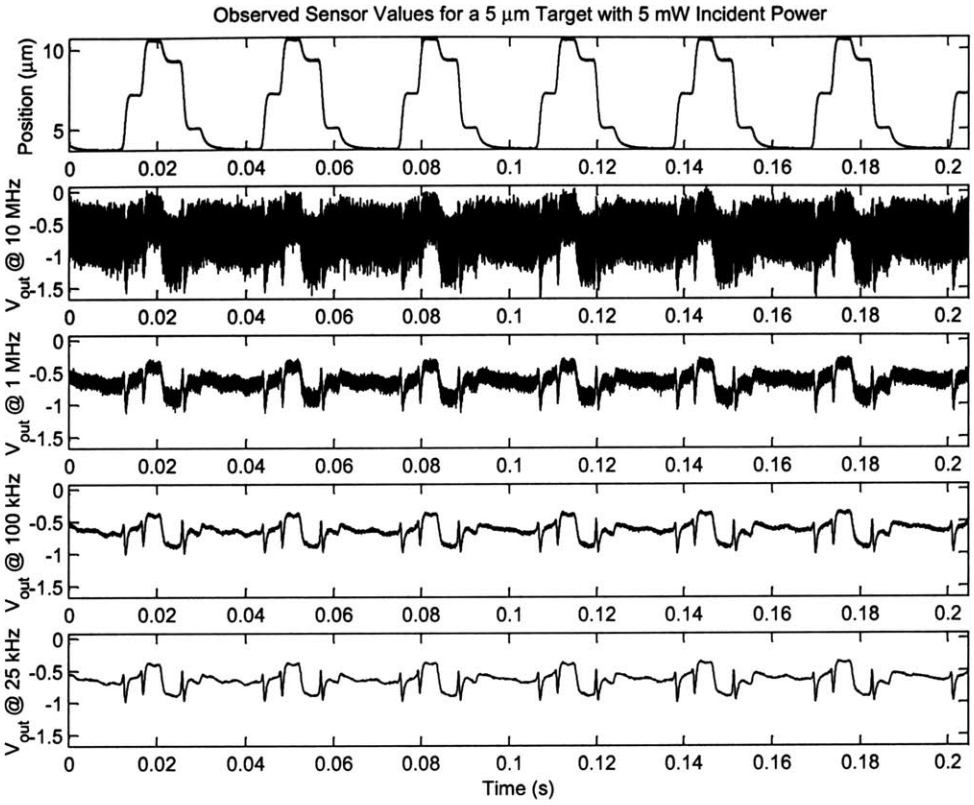

Figure 4-11: Measured data for a 0.5 μm bead experiment. The horizontal axis shows the time sequence of capture. The top trace shows the piezo sensor position corrected for the observed lag, while the lower four traces are band-limited and down-sampled versions of the detected light. As the top trace shows, the stage was driven though a series of rapid steps followed by 4 millisecond rests. The scattered light traces (lower 4 sequences) interleave periods of little change with rapid sweeps through a sinusoidal pattern. Data were acquired at 10 megasamples/s. Approximately 5 mW of power was incident on the slide.

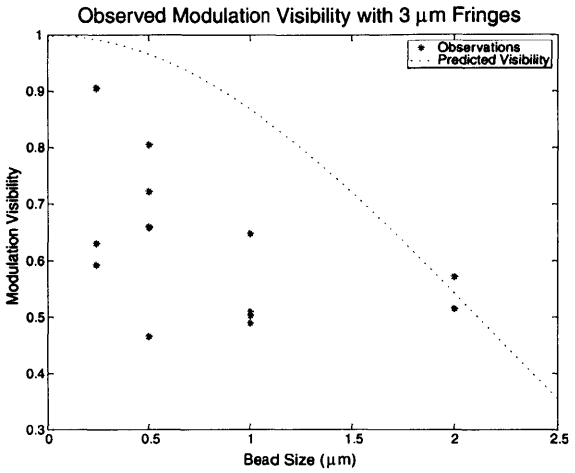

Figure 4-12: Measured modulation visibility. For each setup, a different ratio of output range to maximum output occurred. The dashed line shows the expected visibility based on isolated scattering by one disc in a fringe pattern. The data were taken from experiments with 3 μm fringes and were measured at 1 MHz.

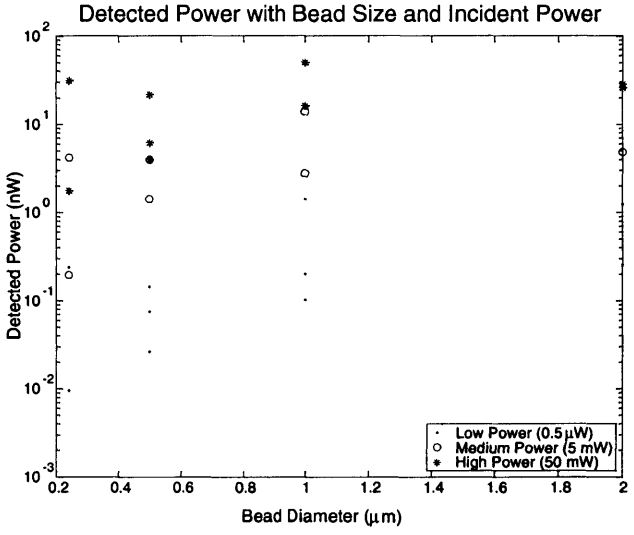

Figure 4-13: Detected power with bead size. The detected power was calculated from the photomultiplier voltage. The legend shows the approximate amount of power incident on the slide during each experiment.

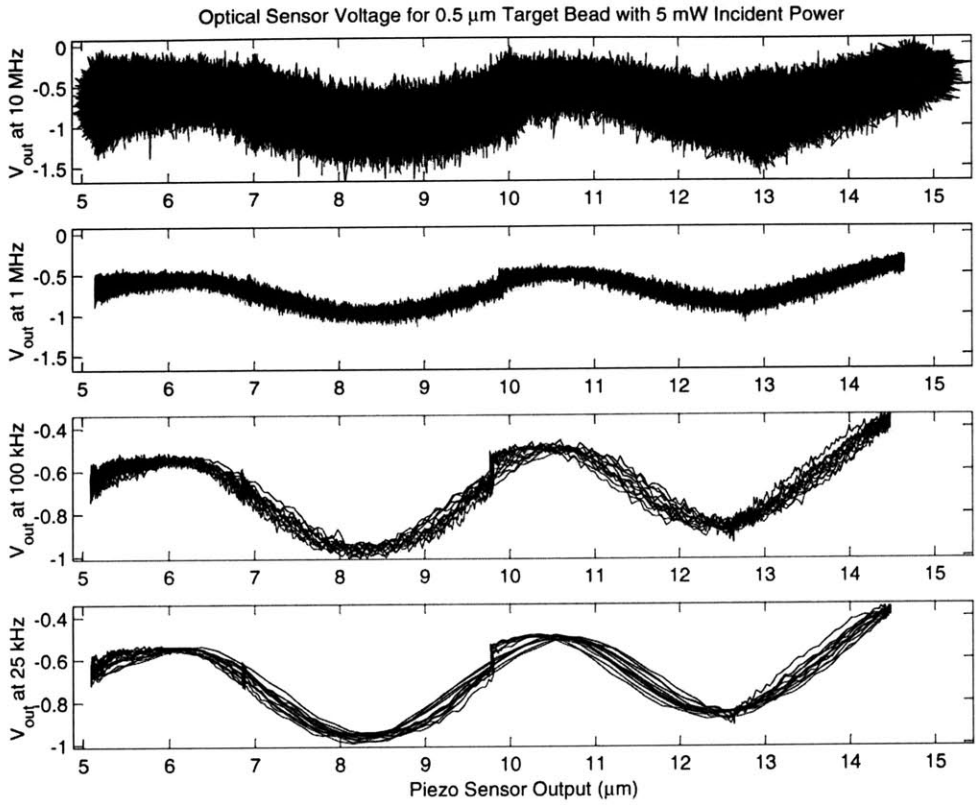

Figure 4-14: Scattering signal with position for a 0.5 μm bead. A 0.5 μm diameter bead was moved through 10 μm through a 3 μm period fringe pattern. The scattered lighted measurements from Figure 4-11 are plotted as a function of the piezo sensor reading at various observation bandwidths. The line sweeps represent the sequence of data acquisition. The sharp vertical jumps in the position traces were found to be consistent with a capacitive delay in the sensor that directly monitored piezo position.

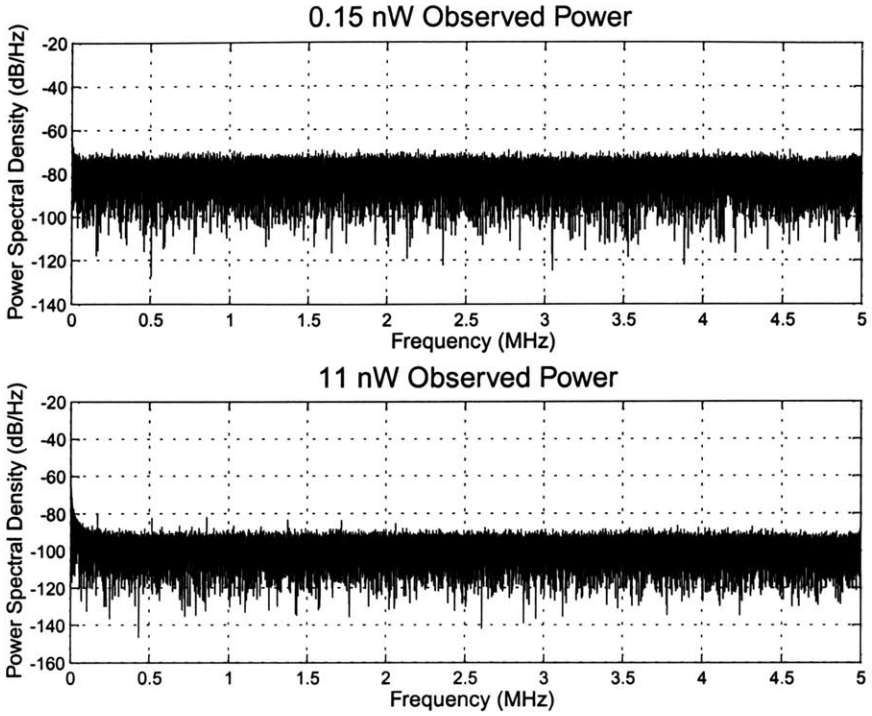

Figure 4-15: Power spectral density of a stationary 1 μm bead. The top figure shows the noise spectrum estimate for a bead with approximately 400 μW of incident power. The lower figure shows the same bead with approximately 70 mW of incident power. The photomultiplier gain adjusted so that the incident power was within the range of measurement.

log-linear least squares fit of the mean rms optical noise on the incident power found that

$$P_{Nrms} \approx 0.23 P_{incident}^{0.48} \tag{4.2}$$

where P_{Nrms} is the rms optical noise level in nW for DC to one megaHertz and $P_{incident}$ was power incident on the photomultiplier as calculated from equation 4.1 (Figure 4-16).

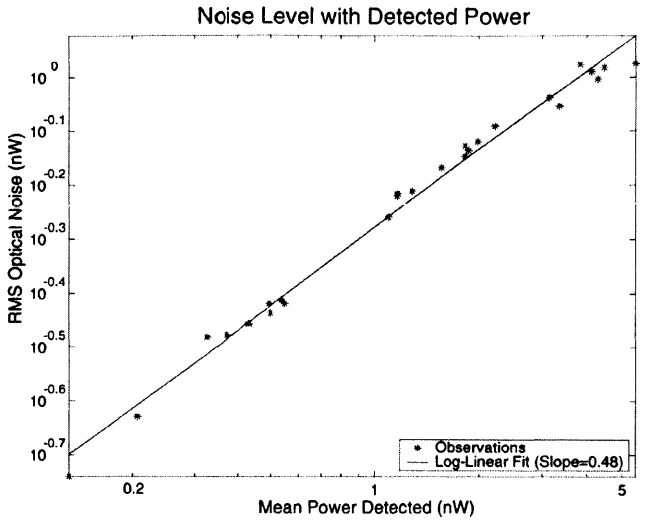

Figure 4-16: Noise power with detected power with a 5 MHz bandwidth. Noise power was calculated from the signal variance with constant incident optical power.

4.5 Discussion

The design of this interferometer provides a platform on which to develop a heterodyne motion detection system. It was able to successfully project fringes with high power density, sufficient contrast, and relatively small spot size. The mechanical layout allowed the angle of incidence to be arbitrarily small, so a high numerical aperture collector lens could be used. With these low incidence angles, primary and secondary reflections of the beams off the slides were not in the cone of observation and did not generate unwanted interference patterns.

A drawback of long working distance of the objective used to project the fringes was the low NA. With an NA of 0.2, the maximum beam separation half angle is 11 degrees so the minimum fringe spacing is 1.22 μm. To achieve smaller fringes, a higher NA objective, along with the corresponding shorting working distance, could be used.

Although the modulation visibility was significantly less than the disc model (Figure 2-1) would predict, all bead sizes achieved greater than 50 percent modulation.

The observed modulation visibility (Figure 4-12) was generally higher for the smaller beads than for larger beads as Equation 2.4 predicted. Additionally, the smaller beads showed greater variance between experiments in the observed modulation visibility.

Undesired scattering particles and stray light are likely causes of this difference in variances. Since smaller beads scatter less light (Figure 4-13), differences in undesired scattered light will cause greater changes in the visibility for small beads than for large beads. The quantity of unwanted scattering particles was controlled as closely as possible, but it was not possible to completely avoid extraneous particles or to maintain a constant level of contamination. These results highlight the need to minimize collection of light from sources other than the target, especially with small beads. The disc theory was shown to provide a useful upper bound on the modulation visibility.

The detected power varied approximately linearly with bead size and with incident power (Figure 4-13) as would be expected with Mie scattering and a linear gain photomultiplier. Within each bead size, the data showed substantial variance. Calibration error of the photomultiplier gain and sample contamination are likely causes of the variance. The photomultiplier gain was sampled at seven control voltages and the means of the samples at each control voltage were best fit to an exponential model (Figure 4-5). The gain was interpolated for the control voltages used during the experiment.

Environmental factors and interpolation errors could cause the estimated gain to differ from the actual gain, and thus cause the reported power to differ by a constant multiplicative factor from the actual incident power. The position determination procedure does not rely on the absolute intensity of power, so these inaccuracies do not effect the accuracy of the result, but the uncertainty makes analyzing the experimental conditions more difficult.

The position versus time diagrams were computed by associating a given "command" sequence of positions with a recording of the observed light. When the light versus time trace (Figure 4-11) was "unwrapped" to correspond to position, the measured data appeared to exhibit a hysteresis. When a bead was traveling in one

direction through the fringes it would follow a smooth curve, but when it traveled the other way it would exhibit a vertical jump (Figure 4-14). It was found that the piezo position sensor was delayed relative to the collected light signal by 153 μs. When the signals were properly delayed, the hysteresis disappeared.

Directly associating collected light intensity with position is one method of detecting motion, but it also demonstrates many of the problems of working with low frequencies. Vibrational and environmental noise cause slow drifts or oscillations in the intensity as evident in the power spectrum of the noise (Figure 4-7). The noise power was up to 30 dB/Hz higher near DC than at 1 megaHertz. When the motion signal in the scattered light oscillations consists of low frequencies, the motion effects are not separable from the effects vibrational and environmental noise.

Chapter 5

Heterodyne Fringe Prototype

The heterodyne fringe motion detection system interferes two beams of slightly different frequencies to form a rolling sinusoidal pattern. In the prototype, the fringe motion is much faster than the bandwidth of detectable target motion, so many cycles of fringes pass over the target during a measurement interval. Unlike the system with static fringes, the target motion of this system affects the phase of the scattered light rather than the amplitude.

5.1 Device Overview

Multiple coherent beams of different frequencies were formed from a single beam with an acousto-optic modulator (AOM). The AOM was driven with a signal composed of two frequencies to produce two first order diffractions. The zeroth and higher order beams were blocked. The optics overlapped and focused the first order beams on a target slide (Figure 5-1). A feedback stabilized piezo was used to investigate the detection system properties by supplying known motions (Figure 5-2), while a second open-loop system stimulated the target at known frequencies with an unknown range of motion (Figure 5-3). A photomultiplier tube mounted on a microscope detected the scattered light. A combination of analog and digital signal processing methods were used to extract the phase modulated motion signal (Figure 5-4).

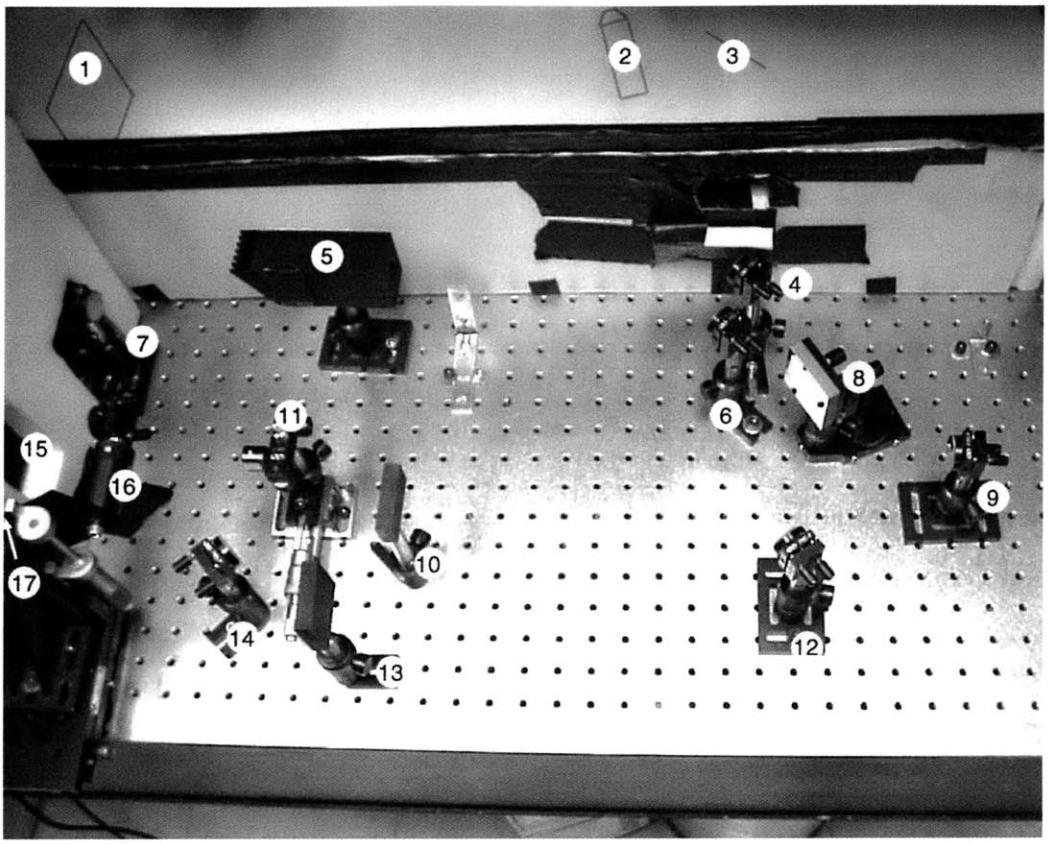

Figure 5-1: Heterodyne fringe prototype optics. An argon ion laser (1) (Inova 304C, Coherent) provided a single coherent beam to the acousto-optic modulator (2) (LS-55, ISOMET). A mirror (3) reflected the beams emerging from the AOM toward the main area. One mirror (4) reflected the zeroth order refraction to a beam stop (5). A different mirror deflected the first (and higher order) beams down the length of the table to another mirror (7) which, in turn, reflected the beams toward another set of mirrors (8 and 9). A large square mirror (8) reflected the beam shifted at lower frequency toward a pair of control mirrors (12 and 14) and finally into a beam splitting cube (11). A piece of black painted Plexiglass (13) stopped higher order beams. The higher frequency beams passed by mirror (8) and were directed by mirror (9) to a beam splitting cube (11). A black painted piece of Plexiglass (10) stopped higher order beams. The beam splitter (11) directed half the energy from both incident beams toward a beam stop (5) and half toward a pair of mirrors that raised the beams (15 and 16). These mirrors centered the beams in an objective (17) within an insulation box that housed the target stage (Figures 5-2 and 5-3).

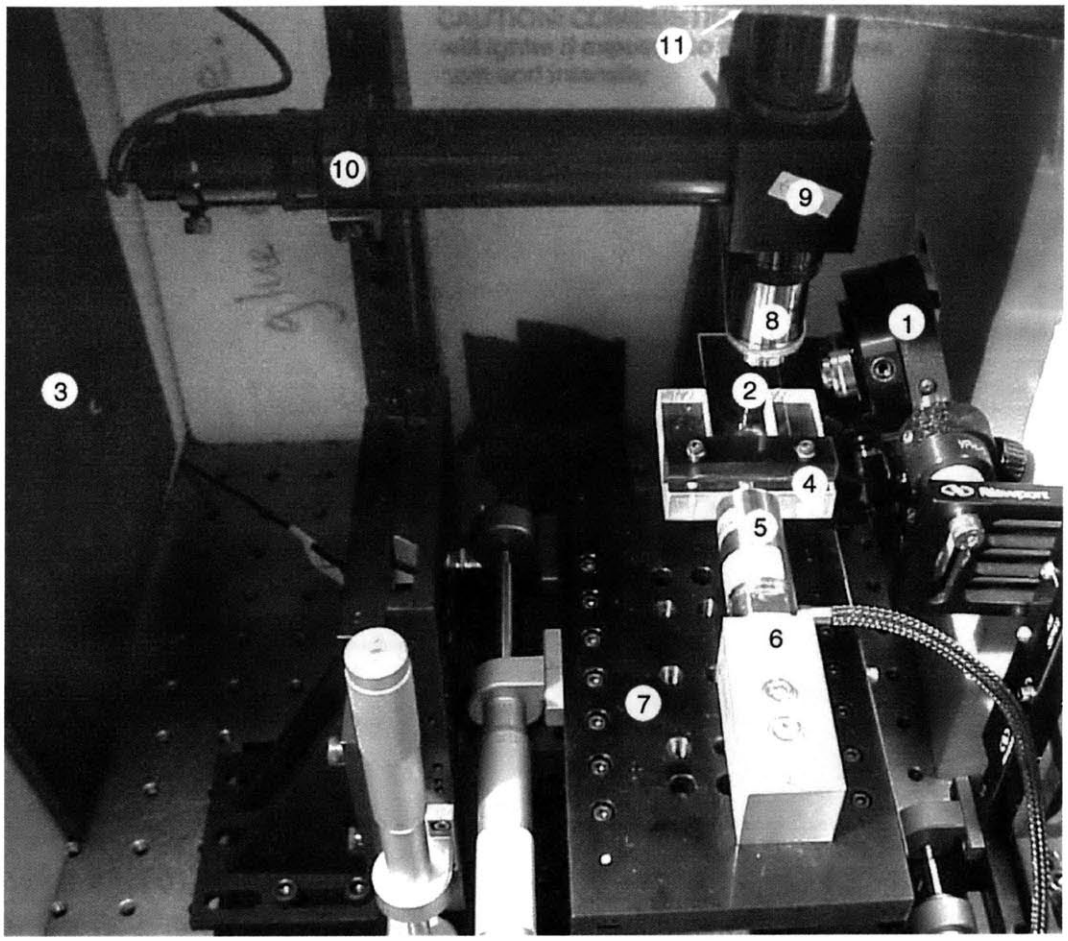

Figure 5-2: Target stage with feedback stabilized piezo. Two beams were overlapped to form a rolling fringe pattern by an objective (1) on a target slide (2). The reflections of the beams off the glass slide were stopped by a black foam board (3). A custom slide holder (4) mounted the slide to the face of a piezo (5) that was mounted to an aluminum block (6). A three axis translation stage (7) allowed precision adjustment and focusing of the slide relative to the microscope objective (8). The microscope (9) was identical to that of the stationary fringe projector with the addition of a 5 mm spacing ring in the optical path of the photomultiplier, a mounting bracket (10) on the CCD camera, and a mounting bracket (11) at the entrance to the photomultiplier (Figure 4-2).

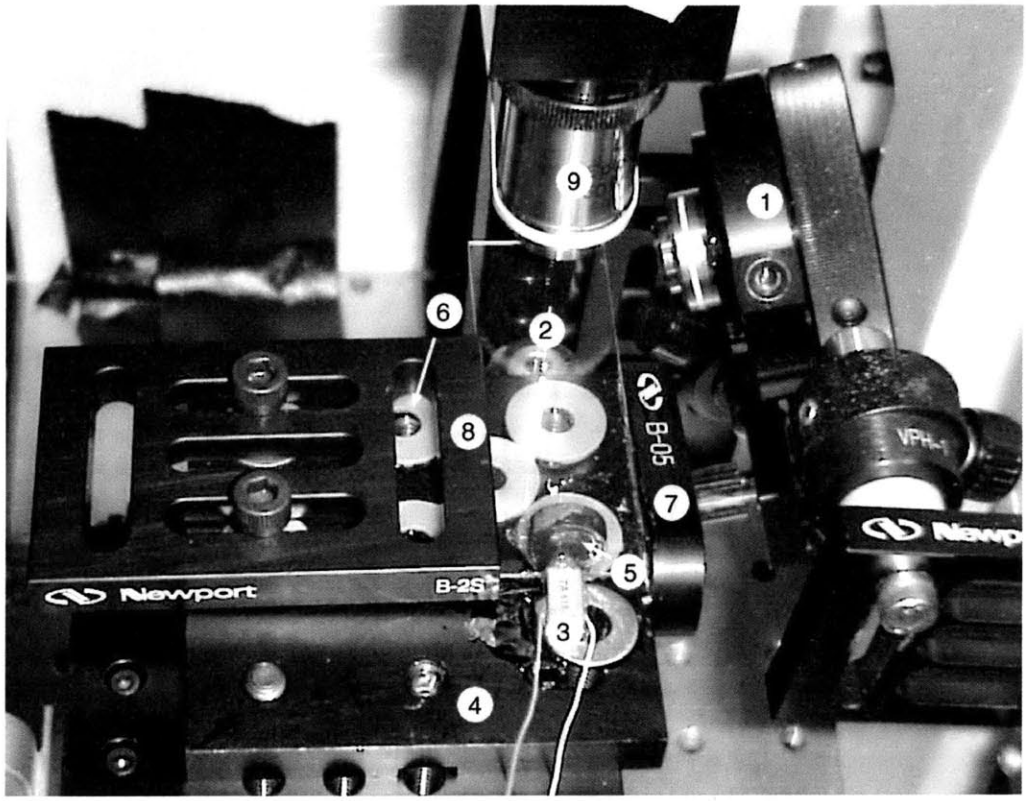

Figure 5-3: Target stage with open-loop piezo. The aluminum block from the feedback stabilized piezo was removed and replaced with a different stage. Beams were delivered to form rolling fringe patterns by an objective (1) on a slide (2). A piezo device (3) stimulated the slide and was epoxied to a base plate (4). A 1 cm magnet (5) was epoxied to the slide and to the magnet mounted on the surface of the piezo. A series of half inch plastic washers (6) provided a linear bearing to reduce friction on the slide. A flat aluminum plate (7) was epoxied to one side of the stage to provide another bearing. A movable base plate (8) was bolted such that it further restrained horizontal motion. The same microscope and detection system (9) were used as in Figure 5-2.

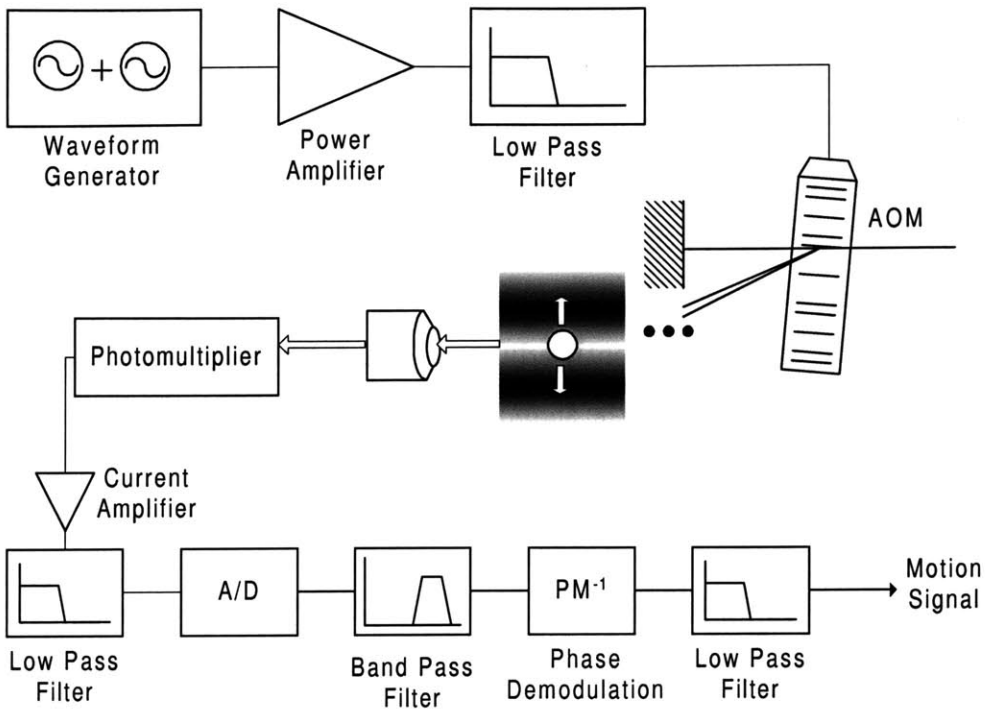

Figure 5-4: Heterodyne prototype signal processing. A two tone drive signal was supplied by a waveform generator (AWG2021, Tektronix) and amplified by a power amplifier (ZHL-5W-1, Minicircuits). A 125 MHz low pass filter (J4239-125M-50-69B, TTE) removed high frequency noise caused by the discrete signal levels of the waveform generator. An acousto-optic modulator (AOM) split a primary beam into two first diffractions that were shifted by driving frequencies of the AOM. The optics system intersected the beams on a target bead to form a rolling fringe pattern. An objective collected light scattered by the bead. A beam splitter directed 30 percent of the light to a CCD for real-time monitoring of bead focus and coarse positioning while 70 percent of the light was collected by a photomultiplier. A current amplifier raised the signal to more easily detectable levels, and a low pass filter band limited the signal for sampling by an analog to digital card. A digital bandpass filter selected the frequency region that contained the majority of the phase modulated content of interest. A digital phase demodulator computed the instantaneous phase. Finally, a low pass filter band limited a scaled version of the motion signal. The actual motion was computed by scaling the phase position by the fringe spacing.

5.1.1 Beam Generation

An acousto-optic modulator (AOM) was used to split and frequency shift the beam. An arbitrary waveform generator (AWG) was used to generate the drive signal that was a superposition of 78.3 and 81.7 MHz sine waves. A custom program controlled the AWG over a GPIB connection and allowed remote control through TCP sockets. The experimental computer controlled the AWG via a custom command line TCP client that was run through Matlab. The drive signal power controlled the diffraction efficiency of the AOM and in turn controlled the amount of power in each first order beam. By adjusting the relative amplitudes of the drive signal component frequencies, each beam intensity was independently adjusted. A high power amplifier followed by a 125 MHz low pass filter prepared the signal from the AWG for the AOM (Figure 5-5).

5.1.2 Fringe Projection and Observation

The angular separation of the first order beams was 2.7 millidegrees, so the beam path was folded to a path length of one meter away from the AOM to allow the diffracted beams to diverge so they could be separately manipulated. The beams were recombined by a beam splitting cube so that they were nearly parallel. The beams were directed into an objective on a three-axis translation stage. The path length from the AOM to the stage was 2.3 meters. By adjusting objective position and mirror angles, the beams were focused on a target bead in the focal plane of the microscope.

5.1.3 Detection and Signal Processing

The design utilized the same photomultiplier, amplifier, low pass filter, and analog to digital card as the stationary fringe prototype. The only change was that the photomultiplier control voltage was supplied by the arbitrary waveform generator so that it could be set from within Matlab. While analog components remained the same, the digital signal processing method was completely different. The detected signal was bandpass filtered around the carrier frequency with a passband twice as

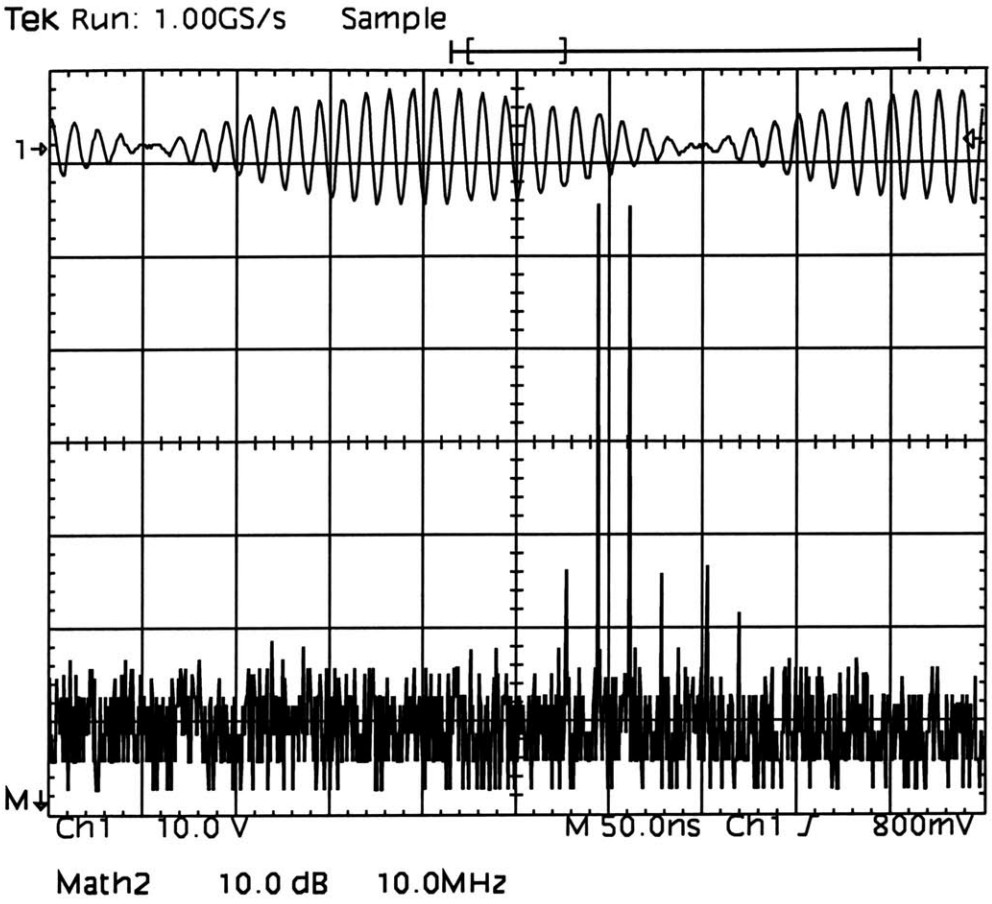

Figure 5-5: Acousto-optic modulator drive signal. The AOM was driven by a superposition of a 78.3 and a 81.7 MHz sin waves at between 2 and 5 volts rms on a 50 ohm load (0.08 to 0.5 Watts). The top trace shows the time signal while the lower trace shows the Fourier transform. Two primary frequency spikes are visible at the drives frequencies.

wide as the desired observation bandwidth. Since the modulated motion signals were generally small, their frequency profiles were largely contained within this interval. Phase demodulation was accomplished by constructing the analytic signal with a Hilbert transform (implemented with fast Fourier transforms). Phase information was extracted from the complex-valued analytic signal, and the phase signal was low pass filtered.

5.2 Calibration

5.2.1 Hardware Interface

The diffraction efficiency of the AOM varied with drive frequency, so the diffracted beams had different intensities when supplied with equal amplitude sine waves. Additionally, the beams traveled different paths and were attenuated to different degrees by the optics. The scattering power from each beam was equalized at the beginning of each experiment by performing a logarithmic search for a ratio of beam powers that provided the same intensity of observed light from both beams.

The photomultiplier gain was also computer adjusted. For each target and laser intensity, a program set the control voltage from Matlab and observed the resulting voltage with the analog-to-digital card. When the amplifier was saturating, it reduced the voltage and when the signal was using less than ninety percent of the possible dynamic range, it increased the control voltage.

5.2.2 Clock Skew

One hardware limitation was that the AOM drive signals were generated on one machine while the detection was done on another. An attempt was made to run the detection system off a clock from the waveform generator, but signal degradation prevented the digital-to-analog card from properly syncing with an external clock. The solution was to use a separate oscillator in each machine. The observed carrier frequency using one oscillator was slightly different (approximately 67.5 Hz on a 3.4

MHz carrier) than the observed frequency using the second oscillator.

In phase demodulation, a miscalculation of carrier frequency results in a linear bias of the signal while in frequency demodulation it results in a constant bias. To compensate for the bias, a time sequence from a stimulated bead was taken and frequency demodulated. It was assumed that the resulting signal would be zero-mean noise since the bead was held stationary. The carrier offset was calculated by assuming the desired signal was zero mean, so that when the observed data was frequency demodulated signal, a non-zero mean was due to carrier frequency miscalculation.

5.2.3 Stimulus Method and Fringe Spacing

During one set of experiments a known motion was applied by the same feedback stabilized piezo system used in the stationary prototype. Since range of motion was known, the fringe spacing was calculated from the programmed movement range. A second open-loop piezo was used to investigate audio frequency sensitivity of the device. In this experiment, the range of motion was unknown so the beams' reflections off the surface of the slide were projected onto a black foam board. The distance between the fringes was measured and angle of intersection was calculated.

5.2.4 Target Preparation

Sample slides were prepared by depositing 20 μL of ethanol on a slide and then placing 1 μL of diluted beads in the ethanol. Beads larger than 0.75 μm were diluted 1,000 to 1 and smaller beads were diluted 1,000,000 to 1. Bead preparations of 2 μm (#19814, Polysciences), 1.5 μm (#17133, Polysciences), 1 μm (#07310, Polysciences), 0.75 μm (#07309, Polysciences), 0.5 μm (#07307, Polysciences), and 0.2 μm (#07304, Polysciences) beads were studied.

5.2.5 Optical Alignment

The objective was moved roughly into place with its three-axis translation stage and one beam was aligned with the target bead. The objective and beam were

slowly adjusted until the observed beam width was minimized. At this point, the focus of the beam was roughly incident on the bead. Then the other beam adjusted with its control mirrors so that it intersected the target. Both beams and objective were then adjusted so that the desired beam separation angle could be achieved. In this experiment, the maximum angle permitted by the numerical aperture of the projection objective was desired.

5.3 Method

For each set of experiments, a bead slide was prepared, mounted and brought to focus. The slide was manually scanned until an isolated bead of representative size was found. The bead was centered in the photomultiplier field of view.

The beams were manually intersected on the target as close to their waists as possible. Each beam was approximately 5 mW when incident on the target slide with a minimum dimension of 50 μm. A custom program adjusted the beam power until the scattering from each individual beam was nearly the same. Typically, the scattering intensities were within 10 percent. Another program adjusted the photomultiplier control voltage to prevent amplifier saturation and ensure adequate use of the voltage bandwidth.

The scattering properties of a variety of different sizes of beads explored by providing a series of known motions with a computer controlled piezo crystal. For each size of bead (0.2, 0.5, 0.75, 1.0, 1.5, and 2.0 μm), a slide was mounted and a bead was isolated. First, the sample was held stationary and 512,000 samples were taken at ten megasamples per second (5.12 ms). Each bead was moved through a series of motions during each of which another 5.12 ms of data were acquired. Finally, the bead was held stationary again. The computer controlled piezo was limited to 250 positions per second, so exploration of audio frequency signals was not possible. The incident power on the slide was varied between experiments by adjusting the amplitude of the AOM drive signal.

In the feedback controlled experiments, the maximum incident power on the slide

was 10 mW. The laser was operated in single frequency mode for long coherence length. The spot was not accurately determined. The minimum dimension of the spot was approximately 50 μm with angle of incidence of about 10 degrees.

During a second set of experiments, the stage was changed and a voltage driven piezo was mounted. A 1.5 μm sample bead was prepared and the lasers were aligned. The angular separation was measured by recording the distance from the sample to a target screen and separation between the reflections off the slide. Angular elevation was calculated by measuring the vertical separation between the beams transmitted through the slide and the reflections. The piezo was driven by a waveform generator (33120A, HP) and an audio amplifier (7550, Techron) that were under manual control.

In the second set of experiments, the laser was operated in multi-line mode for additional power at the cost of a short coherence length. The maximum incident power was 60 mW. The minimum spot dimension was approximately 50 μm and the angle of incident was 6 degrees. The microscope objective was replaced with a 0.6 NA 50x objective (#442851, Zeiss).

In both sets of experiments, the carrier frequency (according to the analog to digital card clock) was determined by frequency demodulating the still bead signals. The mean of this signal was the frequency offset from the attempted carrier frequency. The data were bandpass filtered around the carrier frequency with an equiripple filter [1] with a passband twice the bandwidth of the desired demodulated bandwidth. The bandpass filtered signals were phase demodulated and low pass filtered with an equiripple filter [2]. All processing was performed at a sampling rate of 10 megasamples per second.

[1] 55 dB stop-band attenuation, 632 points, 50 kHz transition band
[2] 20 dB stop-band attenuation, 750 points, 10 kHz transition band

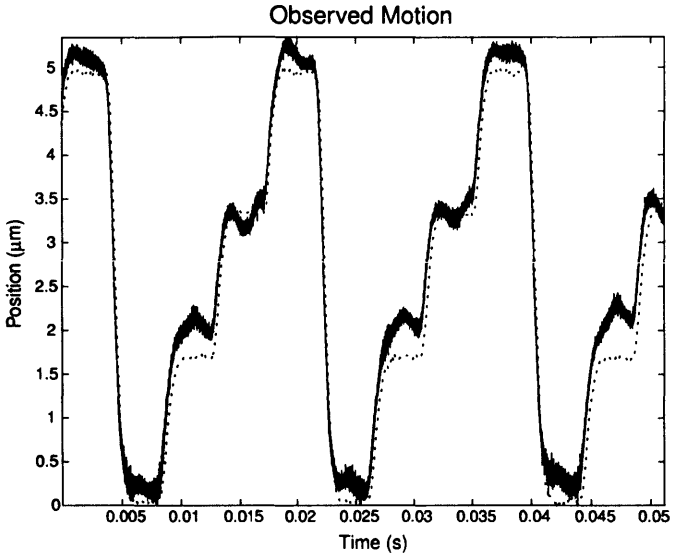

Figure 5-6: Demodulated motion data. The detected motion of the bead (solid lines) exhibited 300 Hz oscillations (as indicated by the small ripples in the trace) in addition to the piezo crystal motion as reported by the capacitive sensor (dotted lines). The signal is bandlimited DC to 100 kHz and was generated using a 2 μm bead in a 3 μm fringe pattern.

5.4 Results

5.4.1 Feedback Controlled Piezo

The observed motion data contained unexpected amounts of low frequency noise in the DC to 500 Hz band (Figure 5-6). The oscillations were present both during stimulus and still measurements. The entire assembly was re-bolted to a vibration dampening table, and the stage was reassembled with sturdier components and additional mounting brackets. The magnitude of the observed oscillations decreased but did not disappear.

Vibration Sensing

A laser Doppler interferometer was used to measure the relative motion of the piezo stage to the objective that delivered the beams. Motions with a frequency spectrum similar to the "noise" spikes were detected (Figure 5-7). Periodic motions on the

order of 400 nm were found with primary frequency components below 500 Hz. The frequency spikes were approximately 20 dB higher than the broadband white noise.

With this verification, it was determined that the detected low frequency noise was uncontrolled motion and not noise from the detection process. As long as the motions of interest were primarily higher frequencies than the table vibrations, separating the signal from low frequency vibrations could be accomplished with filtering. However, in the first set of experiments the vibrations proved problematic since the feedback controlled piezo was roughly bandlimited to 250 Hz.

Comparison of Scattering with Bead Size

The low frequency instability of the stage made determining fringe period problematic. The experiment called for moving the piezo a known amount and measuring the phase change with narrow observation bandwidth (and corresponding low noise). The result was that a significant portion of the noise was concentrated in the low frequencies. Furthermore, the low frequency noise was found to be correlated with the stimulus so averaging over many periods did not substantially decrease the noise, and precise measurements of phase to distance correlations were not possible.

The fringe period was approximated by considering the measured signal to be a superposition of the vibrational noise with the motion signal. The amplitude of the vibrational noise was calculated by recording the detected motion in the absence of stimulus. Then a measurement that contained noise and signal was taken with a stimulus. To determine the amplitude of the non-vibrational motion signal, the amplitude of the vibrational noise was subtracted from the peak-to-peak phase amplitude of the observed signal.

The DC to 100 kHz noise power was found to be on the order of 100 nm (Figure 5-8). Experiments with small beads (and less detectable power) resulted in a wider distribution of noise. The 1.5 μm bead consistently shows approximately 70 nm rms noise.

The broadband white noise was considerably lower than the DC to 500 Hz noise (Figure 5-9). The 0.75 to 1.5 μm beads showed approximately 0.15 nm/$\sqrt{\text{Hz}}$. This

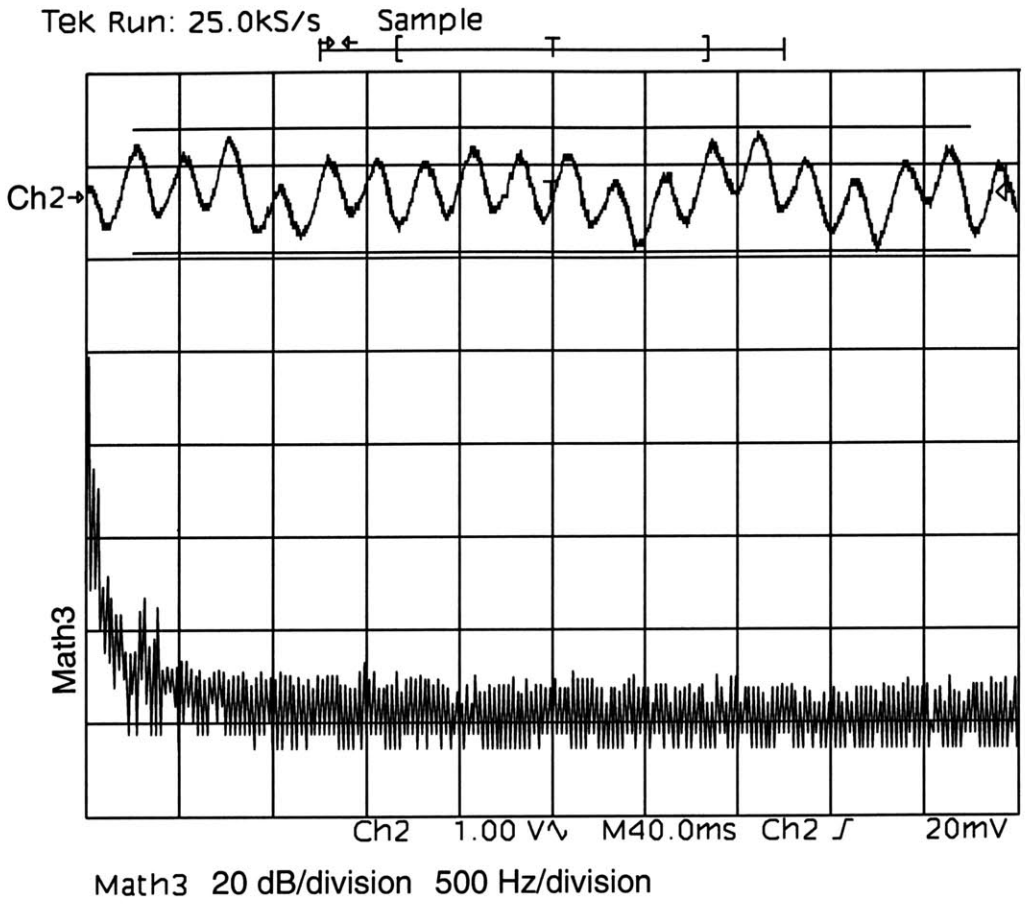

Figure 5-7: Laser Doppler measurement of relative motion between piezo stage and fringe projecting objective. The upper trace (Ch2) shows the displacement with 0.5 μm per division. The local peak to peak amplitude is approximately 400 nm while the peak to peak motion is on the order of 600 nm. The lower trace (Math3) shows the Fourier transform of the displacement signal. The motion has large frequency spikes in the sub-500 Hz region.

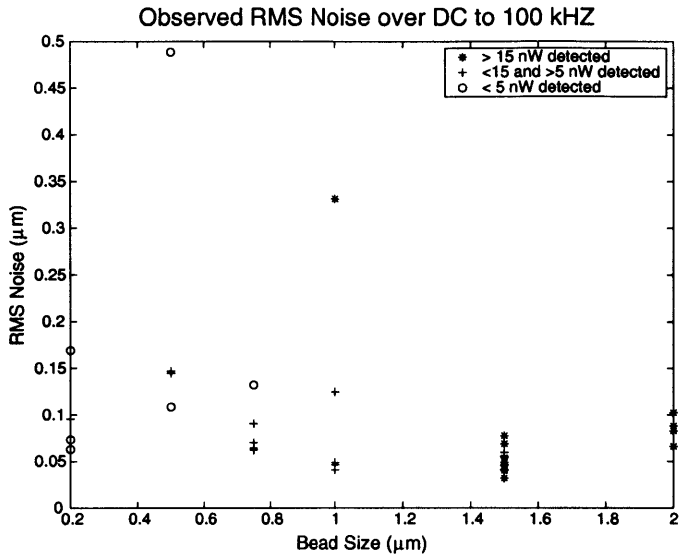

Figure 5-8: RMS noise with bead size for DC to 100 kHz.

would correspond to approximately 50 nm rms over 100 kHz or 150 nm over a 1 MHz bandwidth. The observed amount of noise varied more for smaller beads than larger beads.

The modulation visibility for each bead size was calculated as the amplitude of the bandpass filtered signal over the mean power of the unfiltered signal (Figure 5-10). As with the stationary fringe prototype, the range of modulation depths varied and were less than the theoretical maximum degree of modulation.

5.4.2 Open-Loop Piezo

The open-loop piezo served to stimulate the bead and stage system with known frequency, but unknown amplitude. The maximum frequency of stimulation was limited by the audio amplifier used to drive the piezo. The linear bearings in the stage constrained the motion of the piezo, but off-axis resonance modes appeared for large ranges of movement. The amplitude of drive voltage was adjusted to minimize off-axis vibrations that could be seen with the CCD camera.

The beam separation angle was measured to be 13.9 degrees with a 7.6 degree

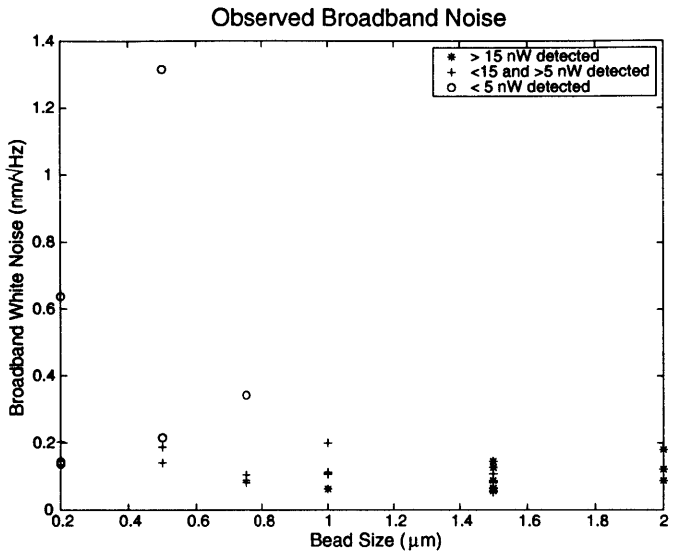

Figure 5-9: Median white noise level for broadband noise above 500 Hz.

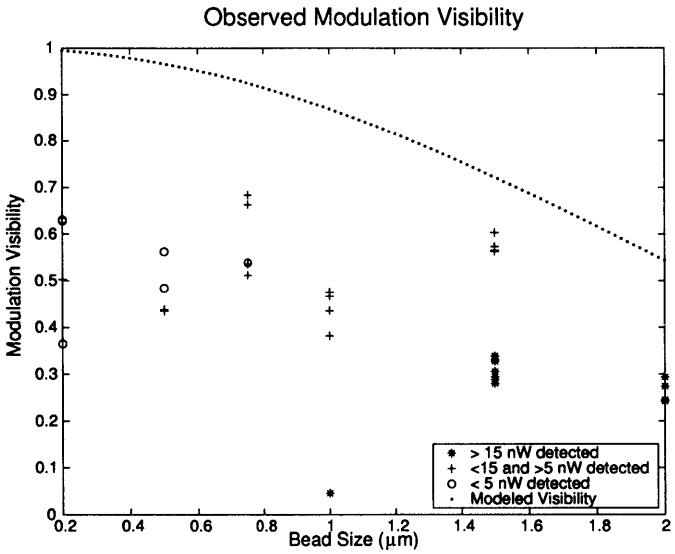

Figure 5-10: Observed modulation visibility.

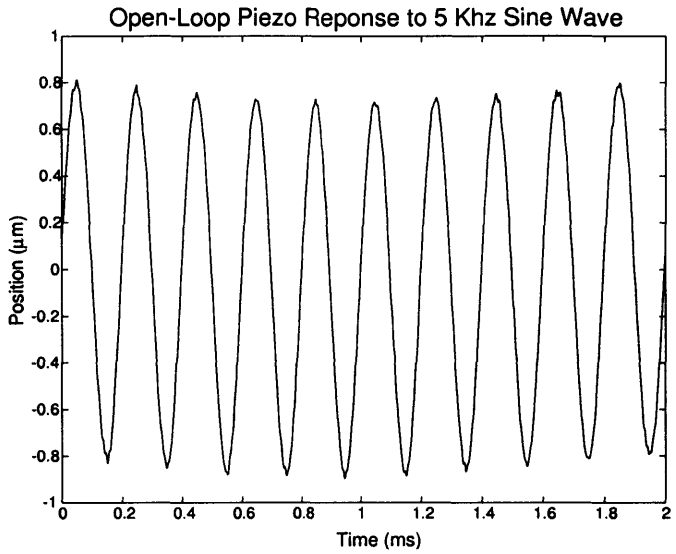

Figure 5-11: Open-loop piezo response to a 5 kHz sine wave. The system oscillated at 5 kHz. Additional low frequency vibrations can seen in the envelope of the sinusoidal motion.

rotation of the beams plane relative to the target slide. The fringe spacing as observed on the slide was 2.04 μm. The samples were bandlimited DC to 100 kHz.

The piezo was driven with a 50 Volt peak-to-peak 5 kHz sine (Figure 5-11). The sub-500 Hz vibrations that were observed with the feedback controlled piezo were also observed. These low frequency vibrations appeared to be less correlated with the stimulus when the system was driven at higher frequencies.

The noise floor of the measurements was calculated by observing the bead while it was not stimulated. Eight 41 ms observations (at 10 megasamples/s) of a still bead were acquired during the course of the experiment. The data were demodulated. The power spectrum of observations showed broadband white noise across the entire frequency range with a noise spike in the 500 Hz band (Figure 5-12).

The mean rms noise from DC to 100 kHz was 32 nm with a standard deviation of 6.2 nm. The mean broadband noise from 500 Hz to 100 kHz was 27 pm/$\sqrt{\text{Hz}}$ with a standard deviation of 2.7 pm. The mean broadband noise from 10 kHz to 1 MHz was 19 pm/$\sqrt{\text{Hz}}$. Extrapolating the DC to 100 kHz rms noise in the absence of the

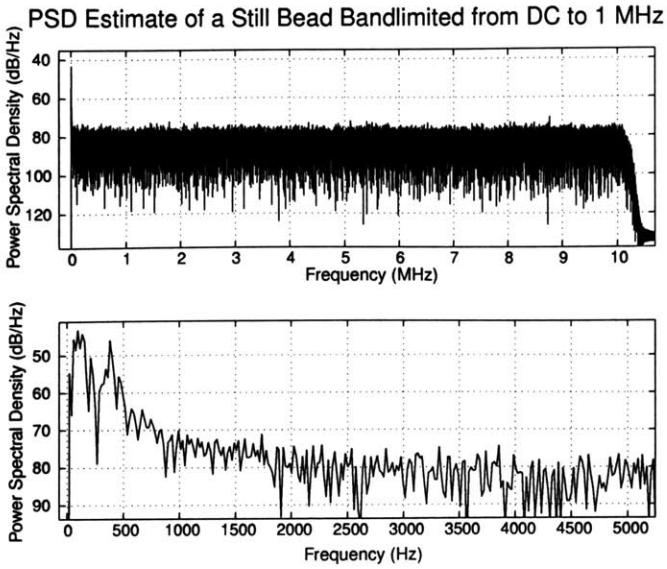

Figure 5-12: Power spectral density estimate of noise in open loop system. The sub-500 Hz noise is 15 dB higher than the broadband white noise.

low frequency vibrations would yield a rms error of 8.5 nm.

The spectrum of the phase modulated content could clearly be seen in the power spectral density of the observed light (Figure 5-13). Phase demodulation utilized only a symmetric band around the carrier frequency, so the motion data were immune to the low frequency noise. The sub-500 Hz vibration noise is evident in the power spectral density of demodulated motion signal (Figure 5-14).

5.5 Discussion

5.5.1 Feedback Controlled Piezo

The laser Doppler measurements of the table motion demonstrated that the low frequency "noise" observed in the analysis was actually motion. It is ambiguous as to whether the slide was moving relative to the optics or the optics were moving relative to the slide. Yet in either case, this noise was not due to the detection process. In future studies, a sturdier mounting method should be used to prevent vibrations. The broadband accuracy of the detection method could still be analyzed with the

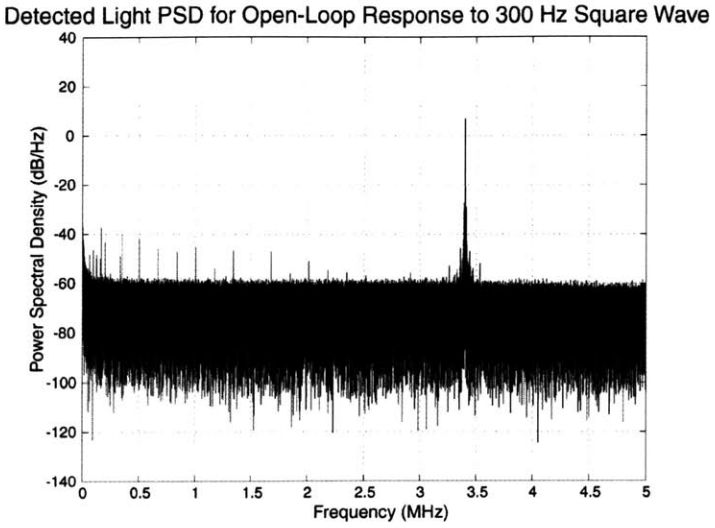

Figure 5-13: Power spectral density of light detected during a 300 Hz square wave stimulus. The motion signal is represented in the frequency band surrounding the 3.4 MHz carrier. Substantial low frequency noise is present in the sub-100 kHz band, but this content was removed by filtering before demodulation.

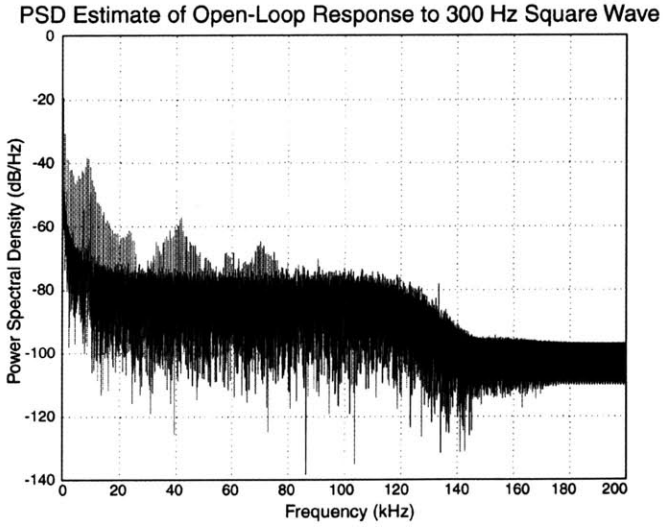

Figure 5-14: Power spectral density estimate of the motion stimulated by a 300 Hz square wave. The spectral peak at 9 kHz represents a resonance frequence of the piezo system. The sub-500 Hz vibrations were the uncontrolled oscillations that were present in all experiments.

existing data even though samples with no colored noise could not be obtained at low frequencies.

The system vibrations corrupted much of the data taken at lower frequencies with the feedback controlled piezo since it could not be determined if the detected difference between the "command" motion of the piezo and the detected motion of the bead were due to actual vibrations or to noise. The method established fringe spacing by correlating absolute phase change with position change. Since the absolute phase contained systematic vibrational errors, the fringe spacing measurements are also not precise. Therefore, the absolute rms accuracy of the measurements are also inexact. Yet, since the targets suffered the same systematic scaling uncertainty from fringe measurements, the relative amount of rms noise between sizes is unaffected by the fringe spacing.

The calculated rms noise from DC to 100 kHz varies more greatly for smaller beads than larger beads (Figure 5-8) and, as scattering model predicted, more power is detected for larger beads. A comparison of the rms noise in the 500 Hz to 100 kHz band reveals that the rms noise is nearly constant at 0.15 nm/$\sqrt{\text{Hz}}$ (500 Hz to 100 kHz) across bead sizes from 0.2 μm to 2 μm despite the large change in the amount of detected power (Figure 5-9. Again, this is consistent with the modeled predictions (Figure 3-5).

The modulation visibility varied substantially within each bead size (Figure 5-10). Generally, the smaller beads exhibited greater modulation visibility than the larger beads, but overall the visibility was less than predicted by the model (Equation 2-1). As with stationary fringe prototype, the largest factor affecting fringe modulation seemed to be the presence of additional scattering particles in the field of view. Care was taken to isolate beads, but some preparations showed many more scattering small particles than others.

5.5.2 Open-Loop Piezo

The open-loop piezo stimulated the targer at much higher frequencies than the closed-loop piezo, so response characteristics composed of significantly different frequencies

from the mechanical vibrations could be studied. The 5 kHz sine wave stimulus clearly shows the low frequency vibration in the envelope of the sinusoid as well as the broadband noise as evident in the small variations near the extrema (Figure 5-11).

The power spectrum of the broadband noise clearly shows a constant level of white noise from 10 kHz to 1 MHz and large spikes at low frequencies (Figure 5-12). Since the low frequency motion of the target was independently verified with a Laser Doppler interferometer, it is reasonable to conclude that the accuracy of the measurement method is limited by the broadband white noise and that the reliability of the stage construction is limited by the vibrations (Figure 5-7).

By measuring the beam reflections on a distant screen, the angle of incidence and beam separation angle could be accurately obtained. Thus, the fringe spacing and accuracy of the system could be reliably calculated. The broadband accuracy of the system was shown to be between 19 pm/$\sqrt{\text{Hz}}$ and 27 pm/$\sqrt{\text{Hz}}$ for 1 kHz to 1 MHz.

If the measured response data are a known to have a definite period (perhaps due to a periodic stimulus) and the noise is not correlated with the measurement, then the rms noise can be reduced. Each measurement may be considered to be an observation of a random variable. If the signal is periodic, then multiple samples are taken at the same point of the signal period and the results can be averaged to reduce the variance.

A bead was stimulated with a 300 Hz square wave and data were acquired for 204.8 ms at 10 megasamples/s. If we assume that the response motion is periodic with the same period as the stimulus, then every observation at a specific point in the cycle is an independent observation of the signal plus noise. In 204.8 ms, there are 61 complete cycles of a 300 Hz wave, so the noise could be reduced by a factor of 7.8 ($\sqrt{61}$).

The existing system can capture up to 16,777,216 samples. With a slight modification of the data acquisition system, the number of samples would only be bounded by the amount of random access memory available in the computer.[3] For periodic motions, many cycles could be acquired and the noise level substantially reduced.

[3]Each 12 bit sample use two bytes of memory during acquisition.

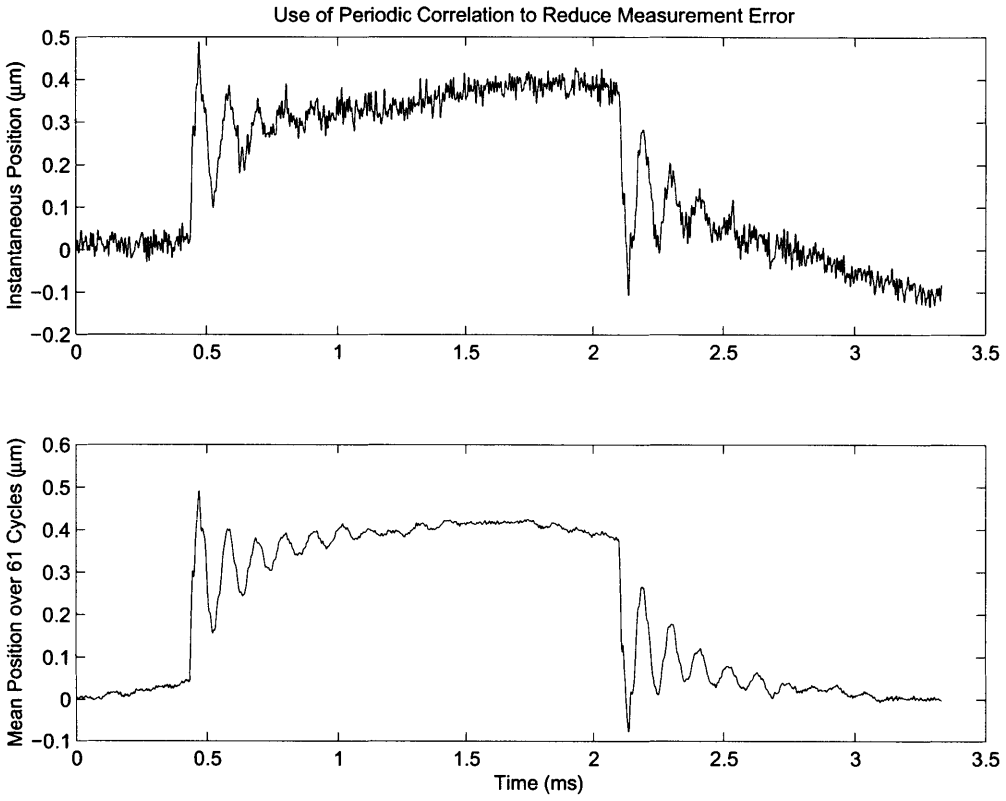

Figure 5-15: Reduction of noise through averaging. The top figure shows a single period of response to a 300 Hz square wave. The rms noise was measured to be 32 nm (DC to 100 kHz). The lower figure shows the mean response over 61 periods. The rms was calculated to be 4.1 nm.

Chapter 6

Closing Remarks

6.1 Heterodyne Fringe Prototype

In this research, we demonstrated a prototype system capable of measuring broadband motions with sub-micron accuracy without exploiting periodic correlations. Although this prototype was not sensitive enough to detect Brownian motion of beads in the tectorial membrane, it successfully demonstrated a broadband motion detection system capable of measuring nanometer movements. Furthermore, the 19 to 27 pm/$\sqrt{\text{Hz}}$ accuracy makes no use of temporal correlation among the data. This system is capable of exploiting temporal redundancy that can lead to vast improvements in the noise floor.

To characterize Brownian motion of a bead, the device would need to sample at least as fast as the characteristic time with at least the resolution of the characteristic distance. An observation bandwidth of at least 2.5 MHz would be necessary to sample motion with a characteristic time of 0.4 μs. The characteristic distance for a 0.5 μm diameter bead is approximately 3 nm. Thus, a mean rms noise level of 1.9 pm/$\sqrt{\text{Hz}}$ would be required. The improvement would need to be a factor of 10 more accurate than the broadband resolution demonstrated. To reliable characterize the Brownian motion of a bead, a factor of 50 improvement would likely be needed.

The limiting factor in the resolution of the prototype was the amount of detected signal power. In short, more light needs to be collected to increase resolution. There

are three possibilities to increase the amount of light collected. A more powerful laser or better optics could increase the incident power density; a bead that scattered more light could be used; or a more efficient method could be developed to collect the scattered energy. Regardless of the method used to increase the amount of collected light, a factor of n increase in resolution requires a n^2 increase in power.

One way of increasing resolution is to increase the power density incident on the bead by using a brighter laser or more tightly focusing optics. The beam diameter used in these experiments was approximately 50 μm, but the beads were only up to several micrometers in diameter. With a different apparatus that allowed higher NA optics and closer working distances, a more tightly focused beam could be delivered. Alternatively, a more intense laser could be used. In this prototype, the AOM diffraction efficiency limited the amount of usable power from the argon laser.

Although the latex beads used in the experiment were convenient and provided safe, cheap scattering particles, other types of particles may have more desirable scattering properties. A material with a greater difference in its index of refraction from that of air (or water) would result in more scattered light. Perhaps metallic spheres of sufficient size could be utilized.

The current design collects at most one percent of the total scattered light. Slightly higher NA lens are available for collecting the light, and new lens may prove to be an incremental improvement. A promising method of improving collection efficiency is to optimize the relative angle between the incident beams and the cone of observation to collect a maximal quantity of the scattered light. Optimizing the apparatus may also involve adjusting the fringe spacing for each bead diameter.[6]

6.2 Future Studies

This prototype only scratches the surface of possibilities for broadband nanosensing with heterodyne interferometry. In particular, this research offers a window into an intriguing possibility that the same approach could be used to measure instantaneous three dimensional positions with the same order of accuracy as in one dimensional

devices.

First, consider a signal model of the one dimensional prototype. Two beams (A and B) are overlapped on a target to form a fringe pattern. Let the frequency of A be f_A and the frequency of B be f_B. Let the directions of propagation be k_A and k_B, for A and B respectively. The fringe pattern is formed perpendicular to $k_A - k_B$ and rolls at a rate of $f_A - f_B$. The motion detected is along the vector $k_A - k_B$ and is modulated at $f_A - f_B$.

Consider the case when a third beam of a different frequency and direction (but same polarization) is overlapped in the target area. Let the third beam be C with frequency f_C and direction k_C. Each pair of beams will form a rolling fringe perpendicularly between them. The resulting illumination pattern will be the superposition of the pair-wise fringe patterns. The motion of the bead along $k_A - k_B$ will be modulated at $f_A - f_B$; the motion of the bead along $k_B - k_C$ will be modulated at $f_B - f_C$; and the motion of the bead along $k_A - k_C$ will be modulated at $f_A - f_C$. As long as k_C is out of the plane $k_A - k_B$, the scattered light will contain motion from three degrees of freedom. If the three frequencies are chosen such that the spacing between them is greater than twice the bandwidth of the motion signal, then aliasing will not occur.

6.3 Conclusion

Broadband laser interferometry is an exciting, evolving field that expands the range of applications of laser interferometry. This technique allows interferometric methods, which have been limited to narrow band measurements, to sense broadband motions. With improvements in the scattering properties of beads and increases in the incident power density, the resolution of these methods may be enhanced to measure the properties of the tectorial membrane.

References

[1] Shunya Inoué. *Video Microscopy.* Plenum Press, New York, 1986.

[2] C. Quentin Davis and D.M. Freeman. Using a light microscope to measure motions with nanometer accuracy. *Optical Engineering*, 37:1299–1304, 1998.

[3] L.E. Drain. *The Laser Doppler Technique.* John Wiley and Sons, New York, 1980.

[4] Amnon Yariv. *Optical Electronics in Modern Communications.* Oxford University Press, New York, fifth edition, 1997.

[5] T. J. F. Buunen and M. S. M. G Vlaming. Laser-doppler velocity meter applied to tympanic membrane vibrations in cat. *J. Acoust. Soc. Am.*, 69:744–750, March 1981.

[6] S. M. van Netten. Laser interferometer microscope for the measurement of nanometer vibrational displacements of a light-scattering microscopic object. *J. Accoust. Soc. Am.*, 83:1667–1674, April 1988.

[7] Y. Yeh and H.Z. Cummins. *Applied Physics Letters*, 4:176–178, 1964.

[8] C. Cameron Abnet and Dennis M. Freeman. Deformation of the isolated mouse tectorial membrane produced by oscillatory forces. *Hearing Research*, 144:29–46, 2000.

[9] H.C. van de Hulst. *Light Scattering by Small Particles.* Dover Publications, New York, 1981.

[10] David Barnett. Mie scattering toolbox. http://www.lboro.ac.uk/departments /el/research/optics/matmie/, May 2001.

[11] Stanford Goldman. *Frequency Analysis, Modulation, and Noise.* McGraw-Hill Book Company, Inc., New York, 1948.

[12] Physical Therapy Department Northeastern University. The auditory system. http://www.ptd.neo.edu/Neuroanatomy/Cyberclass/Auditory/, July 2001.

[13] Dennis M. Freeman. Cochlear mechanisms. http://umech.mit.edu/hearing, May 2001.

[14] Thomas Fischer Weiss. *Cellular Biophysics: Transport*, volume 1. MIT Press, Cambridge, MA, 1996.

[15] S. Timoshenko and J. Goodier. *Theory of Elasticity.* McGraw-Hill Book Company, New York, third edition, 1970.

[16] Craig F. Bohren and Donald R. Huffman. *Absorption and Scattering of Light by Small Particles.* Wiley-Interscience Publications, New York, 1998.

[17] D. L. Felkman. Design and implementation of a high-speed solid-state acousto-optic interference pattern projector for three-dimensional imaging. Master's thesis, MIT, 1999.

[18] S. Hanson. Broadening of the measured frequency spectrum in a differential laser anemometer due to interference plane gradients. *J. Phys. D: Apply. Phys.*, 6:164–71, 1973.

[19] H. Kogelnik and T. Li. Laser beams and resonators. *Applied Optics*, 4(10):1550–1567, October 1966.

[20] J. Stahle, L. Hogberg, and B. Engstrom. The laser as a tool in inner-ear surgery. *Acta Otolaryng*, 73:27–37, 1972.

[21] R. J. Adrian and K. L. Orloff. Laser anemometer signals: visibility characteristics and application to particle sizing. *Applied Optics*, 16:677–684, March 1977.

[22] W. M. Farmer. Measurement of particle size, number density, and velocity using a laser interferometer. *Applied Optics*, 11:2603–2612, November 1972.

[23] G. Bekefi and A. H. Barrett. *Electromagnetic Vibrations, Waves, and Radiation.* The MIT Press, Cambridge, MA, 1977.

[24] M. Born and E. Wolf. *Principles of Optics.* Cambridge University Press, MA, seventh edition, 1999.

[25] S. M. van Netten and B. A. Kroese. *Dynamic Behavior and Micromechanical Properties of the Cupula.* The Mechanosensory Lateral Line: Neurobiology and Evolution.

[26] F.A. Jenkins and H.E. White. *Fundamentals of Optics.* McGraw-Hill, New York, 1957.

[27] Baylor College of Medicine. The Bobby R. Alford Department of Otorhinolaryngology and Communicative Sciences. Review of anatomy. http://www.bcm.tmc.edu/oto/studs/anat/, July 2001.